Bulletin of Volcanology (2018) 80:33
https://doi.org/10.1007/s00445-018-1199-z

RESEARCH ARTICLE

Deposits, petrology and mechanism of the 2010–2013 eruption of Kizimen volcano in Kamchatka, Russia

A. Auer[1] · A. Belousov[2] · M. Belousova[2]

Received: 24 April 2017 / Accepted: 24 January 2018

Abstract

Kizimen volcano in Kamchatka is well known as a source of highly heterogeneous poorly mingled magmas ranging from dacites to basaltic andesites. In 2010–2013, the volcano produced its first historical magmatic eruption with the deposition of 0.27 km^3 of block and ash pyroclastic flows accompanied by slow extrusion of a 200-m-thick, highly viscous (10^{10}–10^{11} Pa s) block lava flow with a volume of 0.3 km^3. The total volume of erupted magma comprised approximately 0.4 km^3 DRE. We provide description of the eruption chronology, as well as the lithology and petrology of eruptive products. The erupted material is represented by banded dacite and high-silica andesite. The dacitic magma was formed during a long dormancy after the previous magmatic eruption several hundred years ago with mineral compositions indicating average pre-eruptive temperatures of ~ 810 °C, fO_2 of 0.9–1.6 log units above the nickel–nickel oxide (NNO) buffer and shallow crustal storage conditions at ~ 123 MPa. The silica-rich andesite represents a hybrid magma, which shows signs of recent thermal and compositional disequilibrium. We suggest that the hybrid magma started to form in 1963 when a swarm of deep earthquakes indicated an input of mafic magma from depth into the 6–11-km-deep silicic magma chamber. It took the following 46 years until the magma filling the chamber reached an eruptible state. Poor mingling of the two melts is attributed to its unusually high viscosity that could be associated with the pre-eruptive long-term leakage of volatiles from the chamber through a regional tectonic fault. Our investigations have shown that shallow magma chambers of dormant volcanoes demonstrating strong persistent fumarolic activity can contain highly viscous, degassed magma of evolved composition. Reactivation of such magma chambers by injection of basic magma takes a long time (several decades). Thus, eruption forecasts at such volcanoes should include a possibility of long time lag between a swarm of deep earthquakes (indicating the recharge of basic magma from depth) and the following swarm of shallow earthquakes (indicating final ascent of the hybrid magma towards the surface). Due to the high viscosity of the magma, the shallow swarm can last for more than a year. The forthcoming eruption can be of moderate to low explosivity and include extrusion of viscous lava flows and domes composed of poorly mingled magmas of contrasting compositions.

Keywords Eruption mechanism · Pyroclastic flow deposits · Viscous lava flow · Petrology · Kizimen volcano

Introduction

Eruptions of individual arc-type volcanoes are often highly variable with respect to recurrence, petrology and chemical composition as well as their style of eruption (Hackett and Houghton 1989; Young et al. 1998; Ruprecht et al. 2012). Each discrete episode of activity will be a combination of slow processes which act on timescales from decades to several thousands of years (i.e. melt evolution in the magmatic system during dormancy) and fast processes which act on timescales from month to seconds (i.e. unrest and eruption) (Sparks and Cashman 2017). Slow processes are mainly recorded in the petrology and the composition of the erupted products (e.g. Auer et al. 2015), whereas fast processes are detected during geophysical monitoring (Yamamoto et al. 2002; Jolly et al. 2010; Belousov et al. 2015a) and also in petrographic records of decompression-related mineral growth (Métrich et al. 2001; Hammer and Rutherford 2002; Blundy et al. 2006), mineral reactions (Rutherford and Devine 2003; Crabtree and Lange 2011; De Angelis et al. 2015) and vesiculation (Belousov et al.

Editorial responsibility: M. Portnyagin

Electronic supplementary material The online version of this article (https://doi.org/10.1007/s00445-018-1199-z) contains supplementary material, which is available to authorized users.

✉ A. Auer
auer@riko.shimane-u.ac.jp

[1] Department of Geoscience, Shimane University, 1060 Nishikawatsu, Matsue 690-8504, Japan

[2] Institute of Volcanology and Seismology, Piip Boulevard 9, Petropavlovsk 683006, Russia

Published online: 03 March 2018

2002; Lautze and Houghton 2007; Shea et al. 2010). In addition, knowledge of previous eruptive activity allows to interpret the current state of a magmatic system and infer the style of activity during future eruptions (e.g. Nakagawa et al. 2011; Belousov et al. 2015b). A combination of monitoring records and detailed petrological studies are therefore required for an informed interpretation of the active magmatic systems of arc volcanoes (Kilgour et al. 2014). Of particular importance are the effects of shallow magmatic processes on the physical properties of the magma because they have the largest influence on the style of eruption and hence the hazard assessment. On one side of the general spectrum are open magmatic systems, which produce frequent Strombolian–Subplinian eruptions. The erupted magmas are often two-pyroxene andesites (Auer et al. 2015, 2016), which are characterized by relatively low viscosities and low water content (Kilgour et al. 2013). Their magmatic systems are described as extensive mush columns within the crust rather than one discrete magma chamber (Dahren et al. 2012). At the other end of the spectrum are relatively closed systems with long recurrence intervals that erupt highly evolved, hydrous magmas, such as amphibole-rich dacites (e.g. Scaillet and Evans 1999). Most of latter magmas produce either Plinian or Pelean (extrusive) eruptions. The difference between two end-members is most likely attributed to the volatile behaviour in the shallow magma system (Martel et al. 1998). In cases where there is no evidence for pre-eruptive degassing, explosive–effusive transition can be also controlled by injection and admixing of recharge magma into the shallow silicic magmatic system (Ruprecht and Bachmann 2010). Recently, it has also been suggested that persistent passive degassing itself could foster magma replenishment and even trigger new eruptions (Girona et al. 2014, 2015).

Kizimen volcano is known as a source of highly heterogeneous, poorly mixed magmas ranging in composition from dacites to basaltic andesites (Piip 1946; Melekestsev et al. 1995). Petrological investigations of banded lavas and pyroclasts of its prehistoric eruptions have allowed retrieval of basic information on processes in the shallow magma chamber (Churikova et al. 2007; Browne et al. 2010; Trusov and Pletchov 2011; Churikova et al. 2013a). In 2010–2013, the volcano produced its first historical magmatic eruption with a total erupted volume of 0.4 km^3 DRE (dense-rock equivalent after Pyle 2015). Here, we provide the first detailed petrological and lithological descriptions of the recently erupted pyroclasts and lava. The information obtained on well-preserved magma mingling textures in the erupted products, combined with the overview of the long-term monitoring data of the volcano, has allowed us to propose a model of Kizimen's magma system and a mechanism of its 2010–2013 eruption. Our model provides new insights on the causes of Pelean-type eruptions and will serve for comparison when assessing eruptive mechanisms and hazards on similar volcanoes such as Mt. Unzen (Nakada et al. 1999) and Mt. Sinabung (Nakada et al. 2017).

Geological background

Kizimen volcano (2380 m asl) is located on the eastern margin of the Central Kamchatka Depression. The edifice started to form during the Late Pleistocene–Early Holocene over a basement composed of basaltic lavas of Early Pliocene age intercalated with basaltic and dacitic tuffs (Shantser et al. 1991). The volcano is built over the steep flank of Schapinsky Graben (Fig. 1) with a relative elevation of 2000 m above the edifice base on its west side and only 1200 m on its east side (here, the edifice is buttressed by the Tumrok ridge). The SW–NE trending normal fault of the graben is well expressed as a 100-m cliff traversing the NW slope of the volcano at an elevation of 1100–1300 m asl (Figs. 1 and 2a).

The first geological description of the volcano was made by Piip (1946). The volcanic edifice of Kizimen represents a relatively symmetric cone composed of several lava domes and thick block lava flows, surrounded by an apron of volcaniclastic material. The oldest domes and lava flows are of dacitic and andesitic compositions. The youngest (several hundred years old) and longest lava flows are of basaltic andesite and extend from the volcano summit down to an elevation of 830 m asl (Shantser et al. 1991; Melekestsev et al. 1995). The only historical eruption of the volcano occurred in 1927–1928. The details are not known, but this was probably a rather weak hydrothermal eruption (the youngest prehistoric lava flows of the volcano are covered by thin soil with no ash layers of Kizimen, the soil contains only rare scattered fragments of hydrothermally altered rocks). The volcano has no a well-defined crater; instead, its summit area is occupied by several lava plugs.

A strong persistent fumarole with high concentration of sulfuric gases and temperatures up to 270 °C is located at the NW slope of the volcano at an altitude of 1950 m asl about 400 m below the summit (Figs. 1 and 2a) (Kirsanova et al. 1983). Onset of the fumarolic activity is reported from the year 1825 (Piip 1946). In 1963, an intensive seismic swarm with earthquakes at depths from zero to more than 35 km was registered under the volcano, but no eruption followed (Senyukov et al. 2011). Tephrochronological investigations of the eruptive history were made by Melekestsev et al. (1995), and the petrology of the erupted products before the 2010–2013 eruption was studied by Churikova et al. (2007, 2013b), Browne et al. (2010) and Trusov and Pletchov (2011).

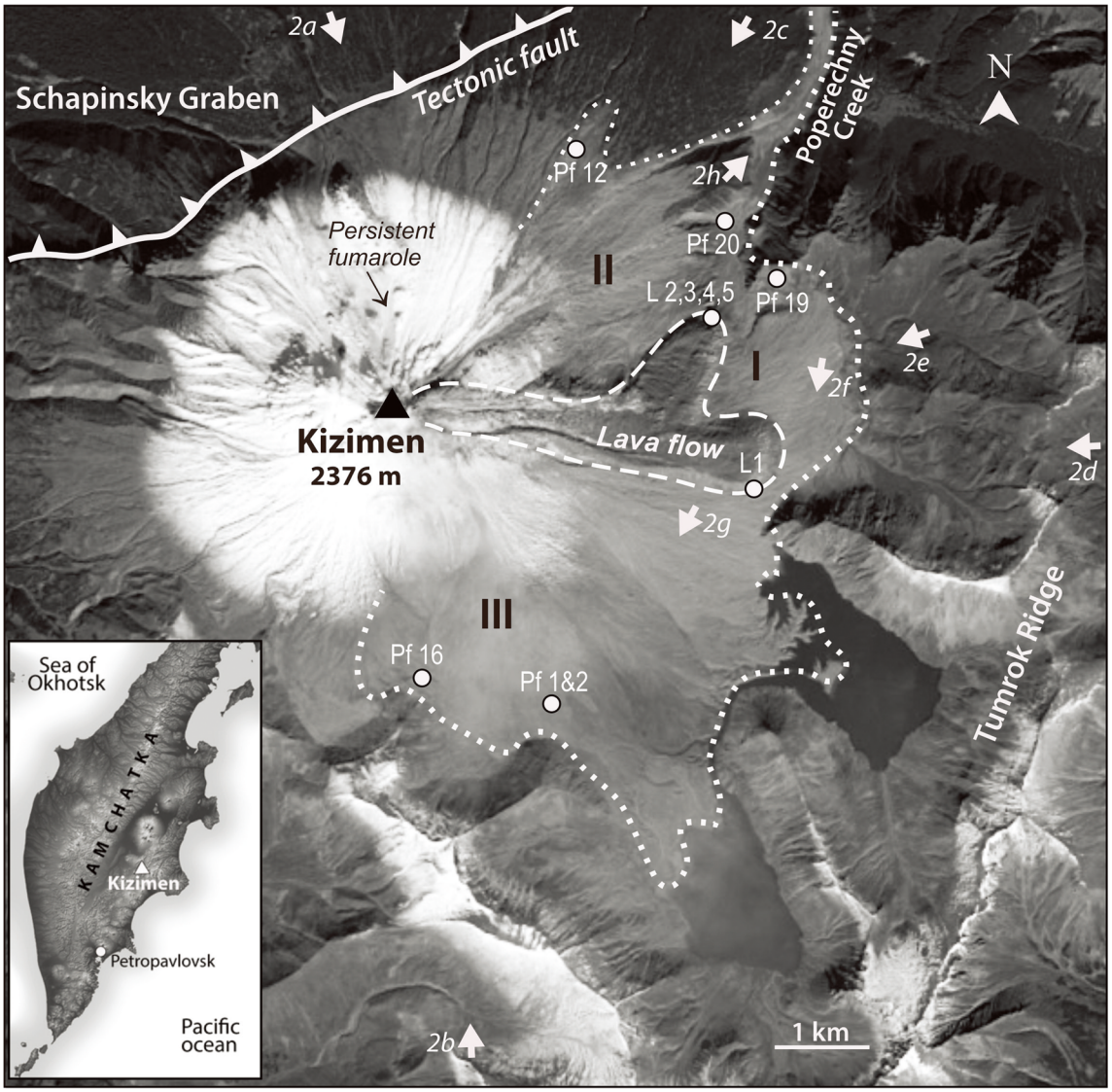

Fig. 1 Sketch map of deposits of the 2010–2013 eruption of Kizimen drawn over the NASA Operational Land Imager acquired on 2 September 2013. Dotted line delineates the areas of the block and ash pyroclastic flow deposit (eastern fan (I), north-eastern fan (II), southern fan (III)). Dashed line delineates the lava flow. White dots with numbers indicate locations of the sampling points of the deposits (PF pyroclastic flows, L lava). White arrows with numbers with letters indicate positions from which photos in Fig. 2 were taken. Inset shows location of Kizimen on the Kamchatka peninsula

Methodology

The description of the eruption chronology represents a review of all the available literature sources on the 2010–2013 eruption, with the addition of our own observations of the eruptive process during our field works at Kizimen in July 2012. The existing visual observations of the initial stage of the eruption are limited because Kizimen is located in a remote region of Kamchatka and is not visible from any permanent settlement. The initial stage was observed mostly by rangers of the Kronotsky Natural Reserve from posts located at distances 14 and 23 km to the W. Unfortunately, these locations provided only a partial view to the eastern slope of Kizimen, where the majority of eruptive events occurred. In July 2011, the Kamchatkan Branch of the Russian Geophysical Survey installed an automatic monitoring camera with the frame rate of one image per minute near Tumrok hot springs located 10 km to the NNE from the volcano (Firstov and Shakirova 2014). From that time on, visual data on the eruption process became more complete.

Velocity of the lava flow was determined using available photographic images of the flow. Velocity of lava at the flow surface was calculated using image sequences obtained by the automatic monitoring camera. Line of sight of the camera was perpendicular to the direction of the lava flow, and positions of large prominent blocks riding on the flow surface could be traced on a succession

Fig. 2 Edifice, the 2010–2013 eruption and deposits of Kizimen volcano. Positions and directions from which photos were taken are indicated on Fig. 1 by white arrows with the corresponding numbers. **a** Volcano from helicopter from NW. **b** Eruption on 10 December 2010, view from S from commercial aircraft, courtesy by Don Page. **c** Eruption on 2 March 2011 with the new lava flow in the summit area, view from NE, courtesy by E. Vlasov. **d** Volcano from the E. **e** Summit extrusion and proximal part of the stagnated lava flow bounded by prominent lateral levees, from NE. **f** Block and ash pyroclastic flow deposit (central part of the eastern fan) with the right branch of the lava flow in the background. **g** Block and ash pyroclastic flow deposit (southern part of the eastern fan). **h** Middle course of the Poperechny Creek filled with the block and ash pyroclastic flow deposit. Vegetation on the flanks of the valley was singed by pyroclastic surges (width of the channel ca. 80 m). Photos **a** and **d–h** by A. Belousov, August 2012

of images with known time intervals. Scale of the images was determined by identification of several characteristic topographic features visible on the volcano slope; the distances between these features were determined by photogrammetic methods (personal communication with V.N. Dvigalo). Surface velocity of lava was calculated as the path travelled by the prominent blocks at the flow surface divided by the time interval between the studied images. Front of the flow was not visible on the images of the automatic camera. Thus, *velocity of the flow front* propagation was determined tracing its positions on a sequence of ASTER satellite images.

Aparent viscosity of lava (η) was calculated using both the flow surface and the flow front velocities (V) by the method of Jeffreys (1925) as first applied to lava by Nichols (1939). The equations $\eta = \rho g h^2 \sin \alpha/2$ V (for flow surface velocity) and $\eta = \rho g h^2 \sin \alpha/3$ V (for flow front velocity) are according to Gauthier (1973). Thickness of lava (h) and slope angle (α) are taken from the maps of the lava flow completed by Dvigalo et al. (2013); g is the acceleration due to gravity, and ρ is the

density of the lava flow as 2300 kg/m^3 (see below). Viscosities calculated using the velocities of the flow front are probably overestimated because frequent gravitational collapses of the flow front made its front velocity less than its theoretical "rheological" velocity. *Yield strength of the lava* was calculated basing on the width of lateral levees of the lava flow (see Harris et al. (2004) for details about the calculation method).

Mapping and sampling of the erupted products was carried out in July 2012 in locations shown on (Fig. 1). In total, 11 samples were collected (Online Resource Table ESM 1). *Density and vesicularity indexes* of rock fragments were determined by the method of Houghton and Wilson (1989) and Hoblitt and Harmon (1993) using the difference between the sample weights in water and air. For the calculation of the vesicularity indexes, the density of both non-vesicular dacite and silicic andesite was taken as 2700 kg/m^3 (Mueller et al. 2011). *Grain size analysis* of samples of the pyroclastic flows was performed by standard dry sieving techniques (Walker 1971). *Componentry analysis* of percentage of different types of rock clasts in the pyroclastic flows was made by visual counting under binocular microscope.

Petrological analysis was performed for all the 11 collected samples of lava and pyroclasts. The samples were manually crushed, cleaned with distilled water and dried for 2 h at 110 °C. The dried fragments were then ground in an agate mortar, and powders were subsequently ignited at 1000 °C for 3 h. Fused disks with a 2:1 flux–sample ratio were prepared using an $LiBO_2$ and Li_2B4O_7 mixture (MERCK) at a ratio of 8:2 (Kimura and Yamada 1996). Glass disks were analysed for major elements at Shimane University with a Rigaku RIX 2000 X-ray fluorescence (XRF) spectrometer. Detailed instrumental configuration and settings are described in Kimura and Yamada (1996). The reproducibility and accuracy of the XRF major element analyses are better than 1.5 relative % (2 s). Modal proportions of all mineral phases have been determined by point-counting based on > 1000 counts per sample. We use the terms phenocrysts (> 200 μm), microphenocryst (> 50 μm) and microlite as descriptive terms for pyrogenic minerals (Dougal and Martin 2008; Crabtree and Lange 2011). In addition, all samples contain glomeroporphyritic aggregates and mafic enclaves, which are described separately and in more detail below. Mineral and glass compositions were determined using wavelength-dispersive spectroscopy (WDS) on a JEOL JXA-8530F field emission electron microprobe analyser with five wavelength-dispersive spectrometers at Shimane University. Analytical conditions were 15 kV accelerating potential, 20 nA beam current with counting times of 20 s on peak and 10 s at the background and a focused beam for oxides and Fe–Mg silicates. A 5 nA beam current and a 5-μm beam diameter (sample/background counting times of 40/20 s) for plagioclase and a 5 nA and variably defocused beam (> 20 μm) for glass to reduce alkali migration (Humphreys et al. 2006b). Sodium and potassium were analysed first, and some larger areal analysis have been performed on exsolution textures and microlite-rich glass to obtain an integrated areal composition. Determination of trace elements during plagioclase line scans required longer counting times (150/90 s for Fe and 300/50 s for Mg). The collected raw data was converted to element wt% by comparison with characteristic standard X-ray peaks using the ZAF matrix correction. Smithsonian microbeam standards NMNH133868, NMNH164905, NMNH143965, NMNH96189, NMNH114887, NMNH 143966, NMNH111312/444, NMNH2566 and NMNH117075 were used for calibration and monitoring of analytical quality. Backscattered electron images have been taken to show mutual mineral relations. Element maps were created using wavelength dispersal spectrometry at 15 kV and 20 nA current, stepped every 1 μm with dwelling times of 80 ms per spot. All amphiboles are calcic and were recalculated based on normalization to 13 cations assuming 23 oxygens (Leake et al. 1997). Fe–Ti oxides were recalculated as described in Carmichael (1967).

The 2010–2013 eruption chronology

The 2010–2013 eruption of Kizimen was preceded by a 1.5-year-long intensive seismic swarm that started in April 2009 (Senyukov et al. 2011). Analysis of the accompanying ground deformations (based on the InSAR data) allowed Ji et al. (2013) to conclude that this swarm was caused by intrusion of a NE–SW trending dike approximately 15 km long and 20 cm thick centred directly beneath the volcano. The dike propagated vertically with a constant rate from a depth of approximately 10 km. A substantial temperature increase of the persistent fumarole at the NW slope of the volcano from 270 to 340 °C in August 2009 was also recorded using thermocouples (Tembrel and Ovsyannikov 2009).

Visual signs of volcano reactivation were first noticed on 16 October 2010 when thermal areas with two new large fumaroles appeared on the snow-covered summit area of the volcano (Melnikov et al. 2011; Senyukov et al. 2011; Malik and Ovsyannikov 2011). On 11 November 2010, periodic ash emissions up to 1 km high started from the fumarole areas and marked the onset of the eruption.

On December 10, the eruption intensity increased notably. This was accompanied by the appearance of a continuous seismic tremor and a persistent thermal anomaly in ASTER satellite images (Senyukov et al. 2011). Frequent ash outbursts accompanied by moderate size pyroclastic flows (PFs) on the eastern slope of the volcano were observed from a passing commercial aircraft

(Fig. 2b) and from the ground (Malik and Ovsyannikov 2011). These "vent clearing" explosions formed a crater of approximately 200 m in diameter that was slightly displaced from the summit towards the eastern slope of the volcano. This crater geometry determined the subsequent eastward path of propagation of the majority of the following PFs and the lava flow.

On December 13, one of the most vigorous explosive episodes of the eruption occurred. According to seismic data, it consisted of a series of explosive events that lasted 20 min (Senyukov et al. 2011). An ash plume with the height of 10 km asl, containing 15.8 kt of SO_2, was detected in Aqua AIRS satellite images (Melnikov et al. 2011). The fallout of fine ash was reported as far as to the Tigil settlement located 310 km NNW from the volcano. These explosions also produced the first major PF of the eruption. The PFs travelled 4.5 km down the eastern slope of the volcano, then collided with the perpendicular western slope of Tumrok ridge and turned northward where they were channelized by a narrow valley of the middle course of the Poperechny Creek (subsequently, all major PFs of the eruption followed this path). Down the valley of the Poperechny Creek, the PFs transformed into voluminous lahars that flooded the valley of the Levaya Schapina river (Malik and Ovsyannikov 2011). The lahars were probably caused by snow melt associated with the emplacement of PFs.

Between 13 December 2010 and the end of December 2011, ash plumes of various heights (commonly accompanied by PFs) were frequently observed both from the ground and in satellite images (Melnikov et al. 2011). According to seismic records, major explosive episodes with formation of significant PFs occurred in chronological order (here all times are in UTC, local time is UTC + 12 h): on 31 December 2010 and 12 and 15 January, 6 to 26 March, 2 May and 31 December 2011 (Senyukov et al. 2011). Ash plumes of these explosions ascended up to heights of 6000–10,000 m asl. Two of these events were especially remarkable. The one on May 2 formed the longest PF of the eruption that travelled 7 km along the valley of the middle course of Poperechny Creek down to the elevation of 500 m asl. This PF was accompanied by a notable ash cloud surge that singed bushes and trees on the steep slopes of the valley (Fig. 2h). Another event on 13 December 2011 produced 16 large PFs and an ash plume of 10,000 m high during 4 h. This plume contained much less SO_2 than the other plumes of the eruption of comparable scale (Melnikov et al. 2011). Footage from the automatic monitoring camera at the Tumrok hot springs area has shown that these PFs and the plume were formed not as the result of explosive activity, but due to gravitational collapses of the advancing front of the lava flow. Total weight of ash fallout deposits since the beginning of the eruption until March 2011 (the period when major volumes of the fallout ash were deposited) was estimated to be approximately 10^7 t (Malik and Ovsyannikov 2011).

In January 2011, simultaneously with the ongoing explosive activity, an extrusion of a rigid lava plug started at the summit crater. By the end of February, lava formed a thick block lava flow 300 m long on the eastern slope of the volcano (Fig. 2c). By September, the length of the lava flow reached 2.5 km with an average thickness of 50 m and a volume of 0.062 m^3 (Dvigalo et al. 2013). According to data of ASTER satellite images, average propagation velocity of the flow front in the period July 3–September 5 comprised 9 m/day (Melnikov et al. 2011). Data of the automatic monitoring camera, in the period from 1 to 7 August 2011, provided the average surface velocity of the lava flow of 50 m/day at the distance of 500–1000 m from the vent. In November 2011, the flow branched towards north-east at a distance of 2.3 km from the vent at an elevation of 1350 m asl. ASTER satellite images indicate that in the period 5 September–11 December 2011, fronts of both branches continued to advance with average velocities of 5.3 and 5.9 m/day for the north and east lobes, correspondingly with an average discharge rate of 16 m^3/s. By 11 December 2011, the thicknesses of lava in frontal areas of the lobes exceeded 220 m and the flow volume was 0.195 km^3 (Dvigalo et al. 2013).

Subsequently, the lava discharge rate started to decrease. From 27 January to 9 March 2012 images of the automatic camera yielded an average velocity of the flow surface of 15 m/day at the distance of 2100–2700 m from the lava source. By June 2012, both branches of the lava flow reached lengths of 1 km and stopped to advance. The total maximum path of the lava flow, that descended from the summit to the altitude of 1130 m asl, reached 3.5 km (Fig. 2d).

After stagnation of the flow, the slow extrusion of a rigid lava plug continued from the summit crater (Fig. 2e). Gravitational collapses of the extruding plug material formed incandescent rock avalanches and small PFs that travelled down the SE (mostly during 2012) or NE (mostly during the 2013) slopes of the volcano. Ash clouds accompanying the largest of these collapses rose to altitudes of about 5 km asl. Increases in seismicity and size of thermal anomaly in ASTER satellite images suggested intensification of the extrusion process during December 2012–January 2013 (Firstov and Shakirova 2014). A slow extrusion continued until December 2013, when the seismic tremor decreased below detection limit indicating that eruption had ceased. Activity of the persistent fumarole on the NW slope of the volcano was not disrupted during the entire eruption and continues to emanate gases at the time of writing.

The 2010–2013 deposits

Pyroclastic flow deposits

Pyroclastic flows of the eruption deposited three major fans: southern, eastern and north-eastern (Fig. 1). All the fans have lengths of approximately 4.5 km because the extent of the PF propagation was limited by the Tumrok ridge, a major topographic obstacle. The largest thickness of the 2010–2013 PF deposits is in the moat between the eastern slope of the volcano and western slopes of the ridge (where the upper course of the Poperechny Creek is located). The largest eastern fan has a maximum thickness of up to 90 m; the medium-sized NE fan is up to 15 m thick, and the southern one is up to 5 m thick. The most voluminous PFs of the eruption in their distal parts were channelized by the deep valley of the Poperechny Creek (Fig. 2h), where PFs formed a narrow, 7-km-long and up to 50-m-thick deposit. The total area covered with PF deposits by 11 December 2011 reached 13.12 km^2 with an average thickness of 20 m and a corresponding volume of 0.265 km^3 (Dvigalo et al. 2013). After that date, the volume of PF deposits increased only negligibly.

The PFs originated from the crater during the first months of the eruption were dominantly of the "boiling over" type, i.e. formed due to a gravitational collapse of non-buoyant, low-energy vertical eruption clouds. Their deposits were buried by later PFs and thus are not accessible now. The later PFs were formed primarily as the result of gravitational collapses of the advancing lava flow front and the extruding summit plug. These deposits are of block and ash type with blocks up to 1–2 m in diameter (some blocks are up to 5 m in diameter) set in lapilli-ash matrix (Fig. 2f–h). The PF matrix is very poorly sorted (Inman sorting 3 phi) and has a polymodal grain size distribution (Fig. 3a). Blocks of the PFs are composed of well-defined bands of light-coloured dacite and light grey andesite (Fig. 4a, b). The rock fragments of the matrix are represented by the same two petrographic types that form the bands in the blocks. The banding textures are ubiquitous and occur on a wide scale ranging from approximately 1 mm to several 10 s of centimetres (Fig. 4a–c). The matrix has a reddish colour due to partial oxidation of some of its rock fragments. The oxidation occurred during the process of lava extrusion preceding the gravitational collapses that formed the PFs. Densities of juvenile rocks (84% of the overall rock fragments) range from 1500 to 2500 kg/m^3 (Fig. 3b). Among them, densities of light grey dacite (57% of the juvenile fragments) range from 1500 to 2200 kg/m^3 with a mode at 1850 kg/m^3, and densities of dark grey andesite (43% of the juvenile fragments) range from 1700 to 2500 kg/m^3 with a mode at 2050 kg/m^3. Vesicularity indexes of light grey dacite range from 18 to 44% with mode at 30%, and vesicularity indexes of dark grey andesite range from 9 to 37% with mode at 24%.

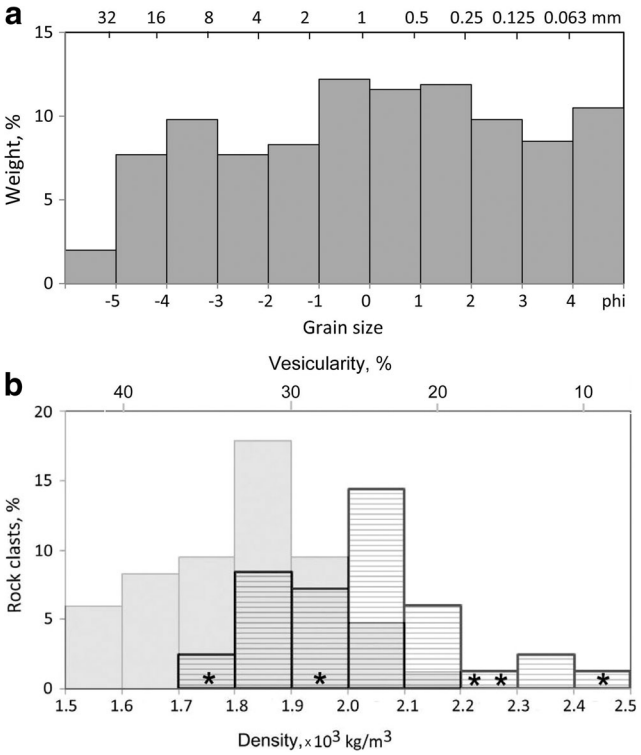

Fig. 3 Representative characteristics of the block and ash pyroclastic flow deposit of the 2010–2013 eruption of Kizimen (sample #PF19 on Fig. 1). **a** Grain size distribution of the PF matrix. **b** Density and vesicularity distribution of 100 juvenile rock fragments. Dacite (grey tone); andesite (striped). Asterisks mark densities of five rock samples from the lava flow

Ash fallout deposits

Deposits of the distal ash fallouts were studied by Malik (2015) and Ponomareva et al. (2012). All the deposits of fallout ash of the eruption are very fine-grained. The < 0.063-mm size fraction (< 4 phi units) comprises 40–70 wt% of the samples irrespective of the distance from the vent. Ash of the initial stage of the eruption (deposited on 10–13 December 2010) was relatively coarse (medium-grained ash) and composed of a mixture of juvenile (fresh glass and crystals) and non-juvenile (altered) rock fragments. These first ash emissions were possibly of phreatomagmatic origin. Ash of the later stages of the eruption is comprised of juvenile particles. Such particularly fine-grained ashes suggest that they were deposited from plumes originated mostly from the co-PF ash clouds (Malik 2015).

Lava flow

The lava flow is of block type (terminology according to Harris and Rowland 2015) with well-defined lateral levees (Figs. 1 and 2d, f). By 11 December 2011, the thicknesses of lava flow in the frontal areas of the two lobes of the flow field were up to 230 m and the flow volume

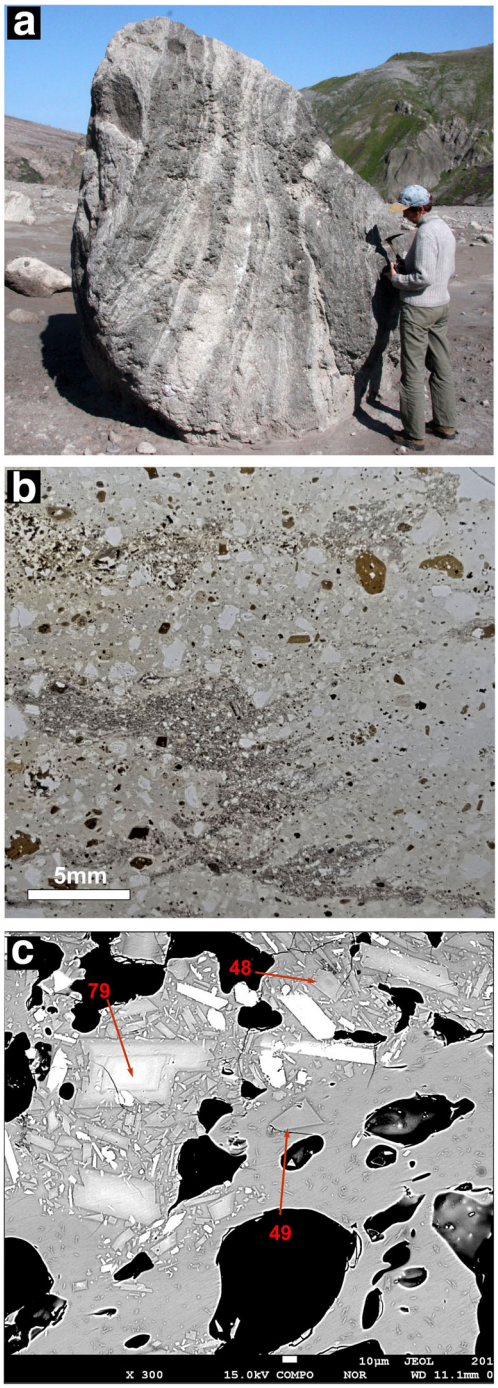

Fig. 4 Andesite-dacite mingling textures on **a** macroscopic scale, **b** microscopic transmitted light image and **c** backscatter image. Numbers denote An# content in groundmass plagioclase (see text for details)

comprised 0.195 km^3 (Dvigalo et al. 2013). Subsequently, by July 2012, the flow increased in length from 2.5 to 3.5 km. No aerial photogrammetric survey was completed after cessation of the eruption, so the final volume of lava can only be estimated based on its area and average thickness, and is probably close to 0.3 km^3. Material of the flow has a reddish colour due to oxidation. Densities range from 1760 to 2420 kg/m^3, and vesicularities range from 10 to 35% (Fig. 3b).

Morphology of the flow and its slow propagation rate indicated extremely high viscosity and yield strength. We used the data on average velocities of the flow front and the flow surface to calculate apparent viscosity of the lava (Table 1). The calculated viscosities are of the order of 10^{10}–10^{11} Pa s. Yield strength of lava comprised approximately 3.3×10^6 N/m^2 basing on the 200-m width of lateral levees of the flow measured on the maps of Dvigalo et al. (2013).

Volume of magma erupted in 2010–2013

The total volume of erupted magma (DRE with density of 2700 kg/m^3) recalculated from the total volume of the erupted pyroclastic flows (approximately 0.265 km^3 with the density of the friable deposit 1500 kg/m^3) and lava (approximately 0.3 km^3 with an average density 2300 kg/m^3) is 0.4 km^3. Volume of the ash fallout deposit is not included in the calculation due to its negligible amount.

Petrology of the 2010–2011 eruption products

Juvenile material of the eruption consists predominately of highly porphyritic, glassy, vesicular scoria. Magma mingling textures are ubiquitous including light grey/dark grey banding features, which range from metre to submillimetre scale (Fig. 4a–c). Dominant phenocryst phases include plagioclase (13–27 vol%), amphibole (1–13 vol%), orthopyroxene (traces 4 vol%), Fe–Ti oxides (1–4 vol%), as well as trace amounts of olivine, quartz and apatite (vesicle free basis). In addition, two types of mafic enclaves are distinguished and will be described in more detail below. The first type includes frequently occurring amphibole-rich aggregates (here named amphibole enclaves) up to 5 mm in size, which also contain plagioclase and subordinate orthopyroxene, Fe–Ti oxides and rare clinopyroxene. The second, less abundant, type hosts cores of olivine, which are always partly replaced by orthopyroxene-magnetite symplectites (subsequently called olivine enclaves).

Whole rock and glass composition

All rocks are medium-K (Gill 1981) silicic andesites and dacites and plot at the boundary of the calc-alkaline/tholeiitic field (Miyashiro 1974). Figure 5 shows whole rock and glass compositions plotted together with results from previous investigations by Melekestsev et al. (1995), Churikova et al. (2013b), as well as distal tephra composition (Kyle et al. 2011). The whole rock chemistry of the

Table 1 Velocity and aparent viscosity of the 2011–2012 lava flow of Kizimen volcano

Time interval (dd.mm.yyyy)	Path (m)	Distance from source (m)	Thickness (h, m)	Slope angle α (°)	Velocity V (m/s)	Viscosity η (Pa s)	Description
1–7 August 2011 (5.5 days)	370	470–840	70	26	5.8×10^{-4}	4.4×10^{10}	Flow surface
3 July–5 November 2011 (63 days)	550	1950–2500	100	11	1×10^{-4}	1.5×10^{11}	Flow front
5 September–11 December 2011 (98 days)	490	2500–3000	120	10	0.6×10^{-4}	3×10^{11}	Left branch front
5 September–11 December 2011 (98 days)	540	2500–3050	150	10	0.7×10^{-4}	4×10^{11}	Right branch front
27 January–9 March 2012 (42 days)	600	2100–2700	125	11	1.6×10^{-4}	2.2×10^{11}	Flow surface

Thickness of lava flow (h) and *slope angle* (α) are taken from the maps of Dvigalo et al. (2013)

recent eruption shows the most evolved compositions in the volcano's record to date. Due to the intricate nature of the banding/mingling textures, a complete separation of the light and dark phase is difficult. Dark and light bands show a range of whole rock compositions between 62 wt% SiO_2 for the dark silica-rich andesitic end-member and 65 wt% SiO_2 for the light dacitic end-member (Table 2, Online Resource Table ESM 2). On a microscopic scale, the banding effects are caused mainly by the abundance of small microphenocrysts and submicron microlites of plagioclase and Ti–Fe oxide minerals (Fig. 4c). The glass compositions for the light translucent glass are almost identical to those reported by Kyle et al. (2011) for the composition of distal tephras from Kizimen. Composition of the dark glass is more variable, and the standard deviation of all analysis is substantially higher (Online Resource Table ESM 2). Nevertheless, the results also show that the dark glasses are overall slightly less evolved. Compositional and textural banding and mingling has been described from many volcanoes worldwide (Eichelberger 1975; Browne et al. 2006; Auer et al. 2015) (Table 2).

Mineral composition, zoning patterns and reaction textures

Plagioclase Plagioclase is the dominant phenocryst phase in all pyroclastic and effusive samples. Major groups of plagioclase are distinguished with respect to their occurrence in the dacitic and andesitic host magma, i.e. dark bands versus light bands (Fig. 6). These include *oscillatory-zoned plagioclase* which occurs as euhedral phenocrysts in the dacitic glass with sizes up to 5 mm (Fig. 6a–c). Zoning patterns are complex but usually more distinct and well defined in the outer rims. Many of the larger plagioclases show cores where zonation is more diffuse or patchy. The overall compositional variation is rather limited with Anorthite content (An#) varying between 44 and 76. Optically distinct compositional zones can reach a high frequency, with there being 50 and more zones within individual crystals; they are therefore very similar to plagioclase populations described elsewhere, for example, at Shiveluch (Humphreys et al. 2006a), Bezymianny (Shcherbakov et al. 2011), Karymsky (Izbekov et al. 2002), as well as at Kizimen volcano itself (Churikova et al. 2013a). *Sieve-textured plagioclase* forms another distinct type of plagioclase but is usually limited to more mafic glass composition/dark bands

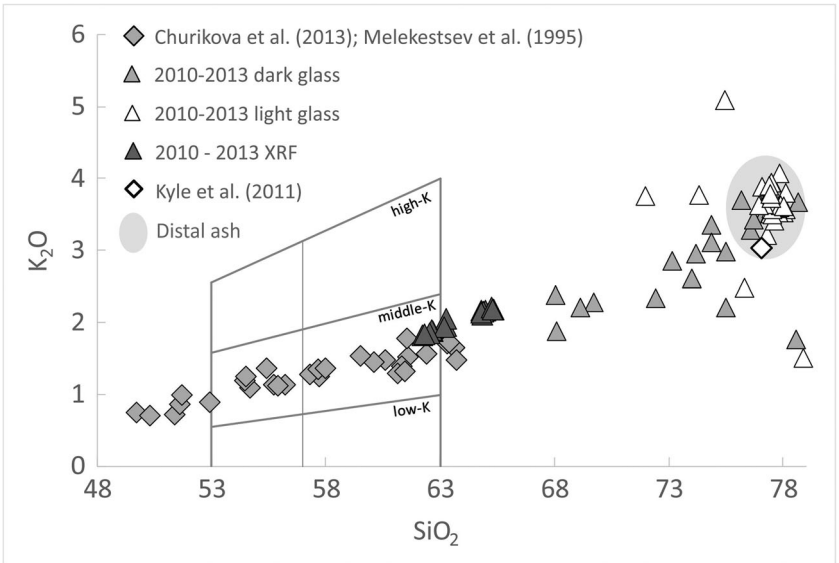

Fig. 5 Geochemical classification of the Kizimen andesites and dacites (Gill 1981). The grey outlined area shows the compositional range of distal tephras (Ponomareva et al. 2012)

Table 2 Whole rock endmember (XRF) and average matrix glass (EPMA) compositions for dark and light mingled domains

Whole rock															Matrix glass	Matrix glass
Sample	PF1A	PF1B	PF2B	PF12AL	PF12AD	PF13L	PF13D	PF16	PF18L	PF18D	PF20L	PF20D	L1	L3	L4	L5	Dark	Light
																	(n = 21; sd = 3.2)	(n = 36; sd = 1.4)
SiO_2	64.97	65.36	62.69	64.79	62.61	64.88	63.26	64.86	64.78	63.26	65.26	62.20	63.19	65.30	62.53	62.29	74.55	77.50
TiO_2	0.73	0.70	0.83	0.74	0.85	0.73	0.80	0.72	0.73	0.81	0.71	0.85	0.80	0.71	0.84	0.84	0.32	0.18
Al_2O_3	15.57	15.70	16.11	15.54	15.99	15.75	16.02	15.93	15.78	15.57	15.69	16.24	16.12	15.65	16.13	16.20	13.25	12.17
FeO	6.72	6.54	7.77	6.82	7.90	6.69	7.52	6.60	6.70	7.65	6.51	8.10	7.44	6.54	7.86	7.88	2.04	1.02
MnO	0.13	0.13	0.14	0.13	0.14	0.13	0.14	0.13	0.13	0.14	0.13	0.14	0.14	0.13	0.14	0.14	0.06	0.04
MgO	1.73	1.68	2.01	1.77	2.05	1.66	1.92	1.68	1.71	1.93	1.61	2.07	1.95	1.68	2.04	2.04	0.62	0.17
CaO	5.97	5.98	6.78	5.97	6.79	6.04	6.60	5.91	5.96	6.86	5.94	6.90	6.55	5.87	6.87	6.94	2.33	1.36
Na_2O	2.29	2.30	2.21	2.32	2.18	2.27	2.22	2.26	2.27	2.21	2.28	2.19	2.22	2.28	2.20	2.19	3.55	3.31
K_2O	2.17	2.18	1.89	2.17	1.90	2.16	1.96	2.11	2.15	2.06	2.21	1.83	1.94	2.18	1.86	1.84	2.94	3.40
P_2O_5	0.14	0.14	0.14	0.14	0.14	0.13	0.14	0.13	0.14	0.14	0.13	0.15	0.14	0.14	0.15	0.15	nd	nd
Total	100.42	100.71	100.57	100.40	100.56	100.44	100.59	100.32	100.35	100.62	100.48	100.68	100.50	100.47	100.61	100.51	99.65	99.15

(Fig. 6d–f, h). Figure 6h shows an example where a small portion of a low An# core is preserved within a resorbed plagioclase. The compositions labelled in the sample represent integrated compositions of a resorbed area (stippled circles). Reaction products in these areas are a new secondary calcic plagioclase and a silica-rich glass with SiO_2 content up to 80%. Textures are characteristic of remelting and similar to those obtained experimentally (Nakamura and Shimakita 1998). All sieve-textured plagioclases have an outer, pristine and unresorbed rim between 60 and 100 μm. This outer rim often shows high An# closest to the resorption zone but subsequently lower An# towards the rim. In some cases, a further outermost anorthite-rich rim has formed (Fig. 6d). Also limited to the andesitic glass/dark bands and relatively rare are plagioclases with variable (or no) internal zonation but with a sharp, well-defined calcium rich rims (Fig. 6g). Groundmass *plagioclase microphenocrysts* in the dark glass show compositions between An#51 and An#84. In contrast, the overall limited number of groundmass plagioclase in the light glass shows lower anorthite content between An#48 and An#66#. Almost all of the small groundmass plagioclases show normal zonation (Fig. 4c) towards more sodic compositions.

Trace element concentrations in plagioclase have been used as a tool to decipher processes prior to eruption as well as to distinguish different magma inputs (Hattori and Sato 1996; Churikova et al. 2007). Iron and magnesium concentrations have been determined for several plagioclases hosted in dacitic/light-coloured bands (Fig. 6a–c) and andesitic/dark grey bands (Fig. 6d–f, h).

Iron concentrations for plagioclases hosted in the dacitic glass are generally below 2000 ppm and show flat equilibrated profiles which are largely independent of the respective anorthite content. Similarly, magnesium concentrations for the dacite-hosted plagioclases generally show concentrations well below 400 ppm and no correlation with Anorthite content (Fig. 7). Similar patterns are also obtained for cores of andesite-hosted resorbed plagioclases (if they are preserved, e.g. Fig. 6h). In contrast, iron concentration in the outer rims of andesite-hosted plagioclase shows significantly higher values between 4000 and 6000 ppm which are correlated with anorthite content. Magnesium concentrations vary between 400 and 1100 ppm (Fig. 7) and show similar compositional trends with initial negative correlation between Mg and An# away from the resorption zone and a subsequently positive correlation towards the outer rim. Sharp outer anorthite-rich rims, as seen in Fig. 6d, g, also show a sharp increase in trace element concentrations.

Plagioclase in mafic enclaves Plagioclase occurs in all mafic enclaves. It shows euhedral to subhedral shapes in most amphibole-rich enclaves with compositions roughly equal to those observed in the sieve-textured plagioclase (An# 43–88). In contrast, plagioclase in olivine enclaves shows euhedral to

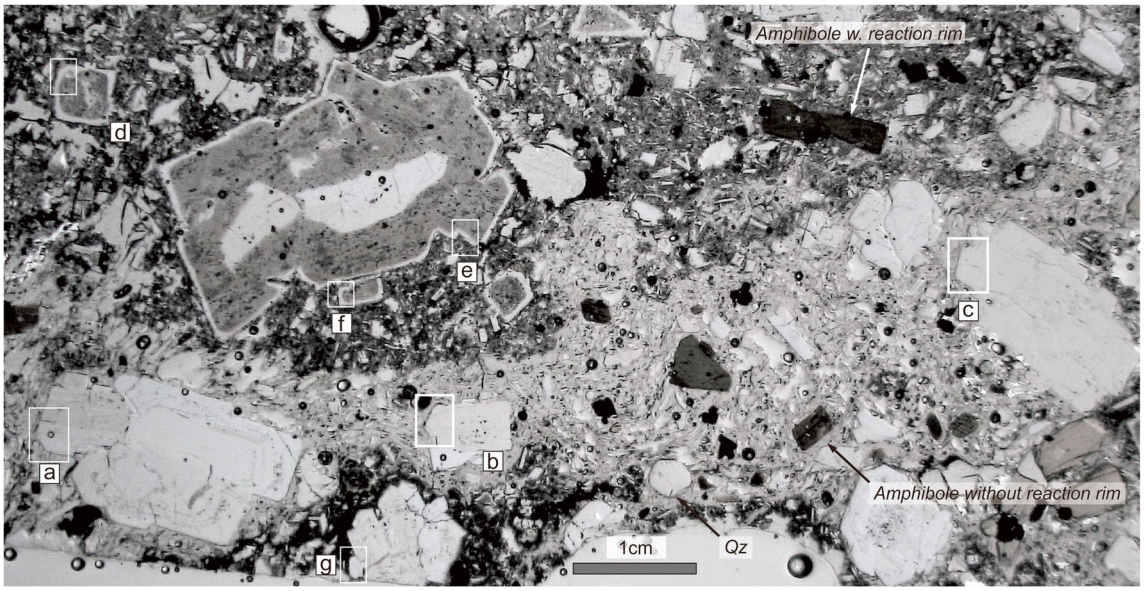

Dacite hosted

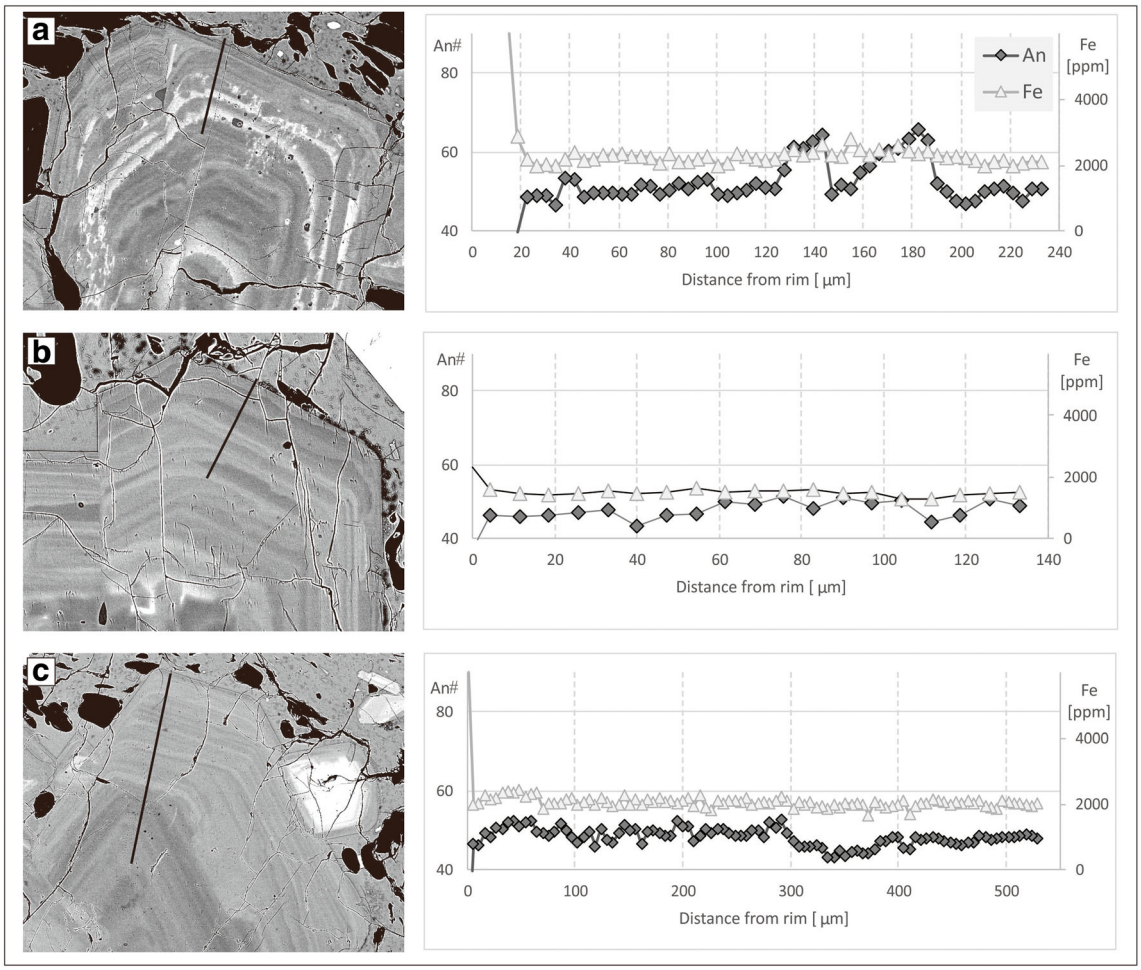

Fig. 6 Overview thin section photograph (plane polarized light) showing a typical banding texture with a light band in the centre part of the image and dark grey bands in the upper part of the image and the lowermost rim. Rectangles indicate phenocrysts chosen for trace element profiles in **a**–**h** (plagioclase 6 h is not visible in the overview image). Notice the petrographical differences of groundmass glass textures between individual domains in backscatter images

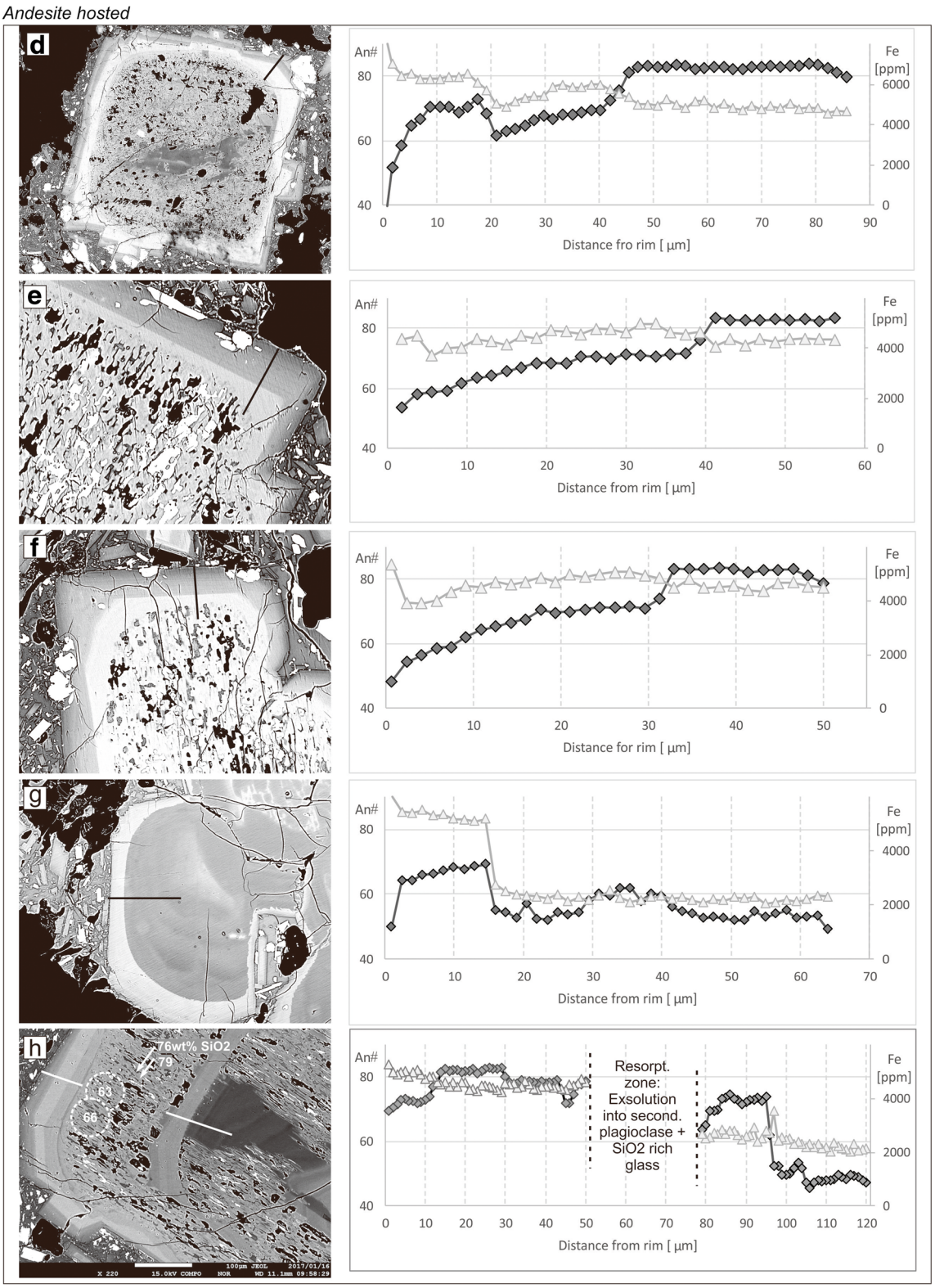

Fig. 6 (continued)

subhedral shapes at the exterior rims of the enclave but completely anhedral shapes within these aggregates (Fig. 8). Conspicuous triangular or polygonal slightly curved, outlines of these aggregates resemble the shape of interstitial spaces between larger mineral grains. The anorthite component in several of these aggregates is well above An# 90.

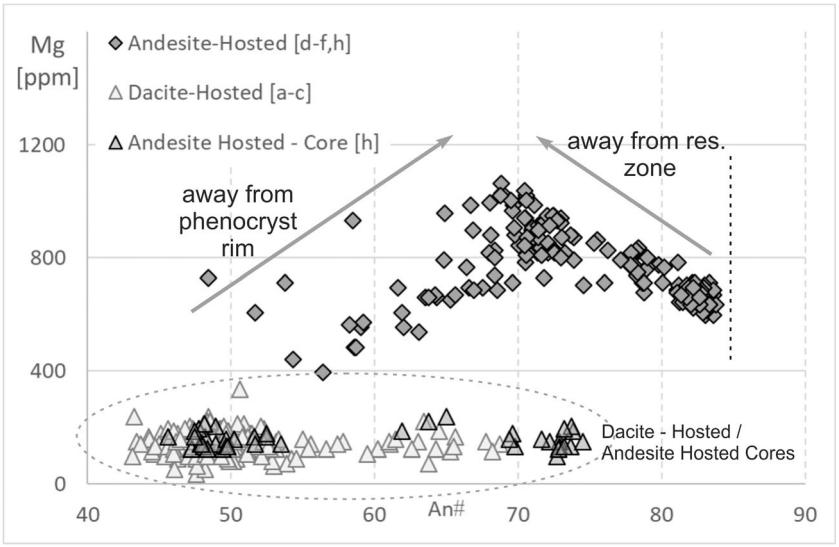

Fig. 7 Plagioclase magnesium concentration vs. anorthite content

Amphibole Amphiboles are the second most frequent phenocryst phase, and three different textural groups are distinguished (Fig. 9a–f). They are classified as tschermakites and magnesio-hornblendes (Fig. 10a, Online Resource Table ESM 2). The first group contains all oscillatory or vaguely patchy zoned amphiboles hosted in dacitic domains (Fig. 9a, b). The overall compositional variations within this group are small and only detectable with high contrast backscatter images. Detailed element concentration maps (Fig. 9b) reveal that the dominant cause of the zonation is related to the overall alumina content, as well as slight variation in ∑A site composition (T-sensitive Edenite exchange and Ti-Tschermak Exchange-Bachmann and Dungan 2002). Amphiboles of the first group show euhedral shapes and are knife sharp with well-defined outer edges without any breakdown rims. Figure 9a, b also shows typical characteristics of the host glass with only a few microphenocrysts and large vesicles with fluidal shapes.

The second group includes amphiboles in the andesitic domains which ubiquitously show breakdown rims of highly variable size (Fig. 9c, d). Besides the occurrence of these reaction rims, their composition is similar to those of the first group (Fig. 10) and they also show vague patchy or oscillatory zoning in their interiors. Breakdown rims comprise varying proportions of pyroxene and Fe–Ti oxides, and thicknesses of the rims can vary between > 1 μm to completely decomposed amphiboles in the late lavas.

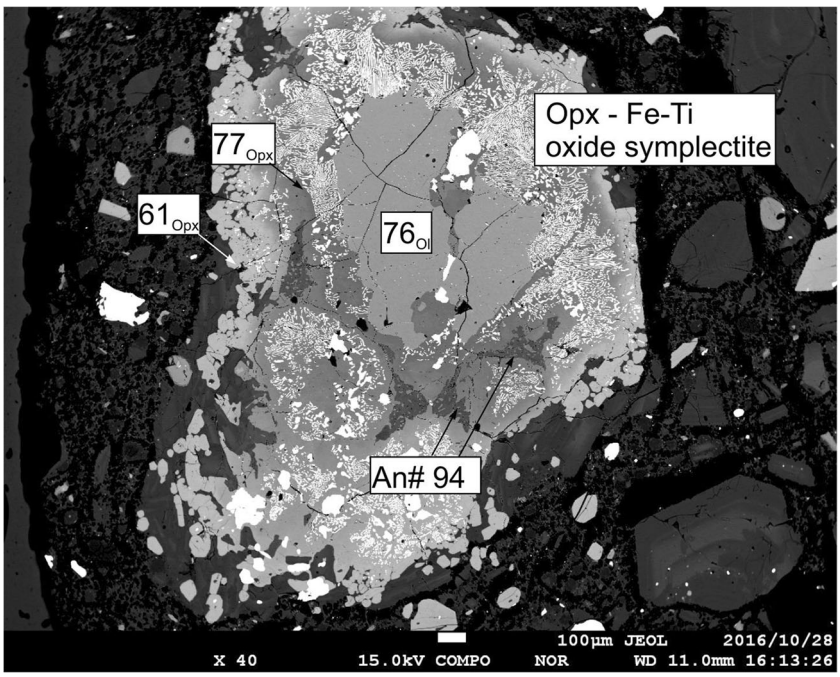

Fig. 8 Mafic enclave showing a core of olivine which is replaced by an orthopyroxene–Fe–Ti oxide symplectite (labels on olivine and pyroxene are magnesium numbers)

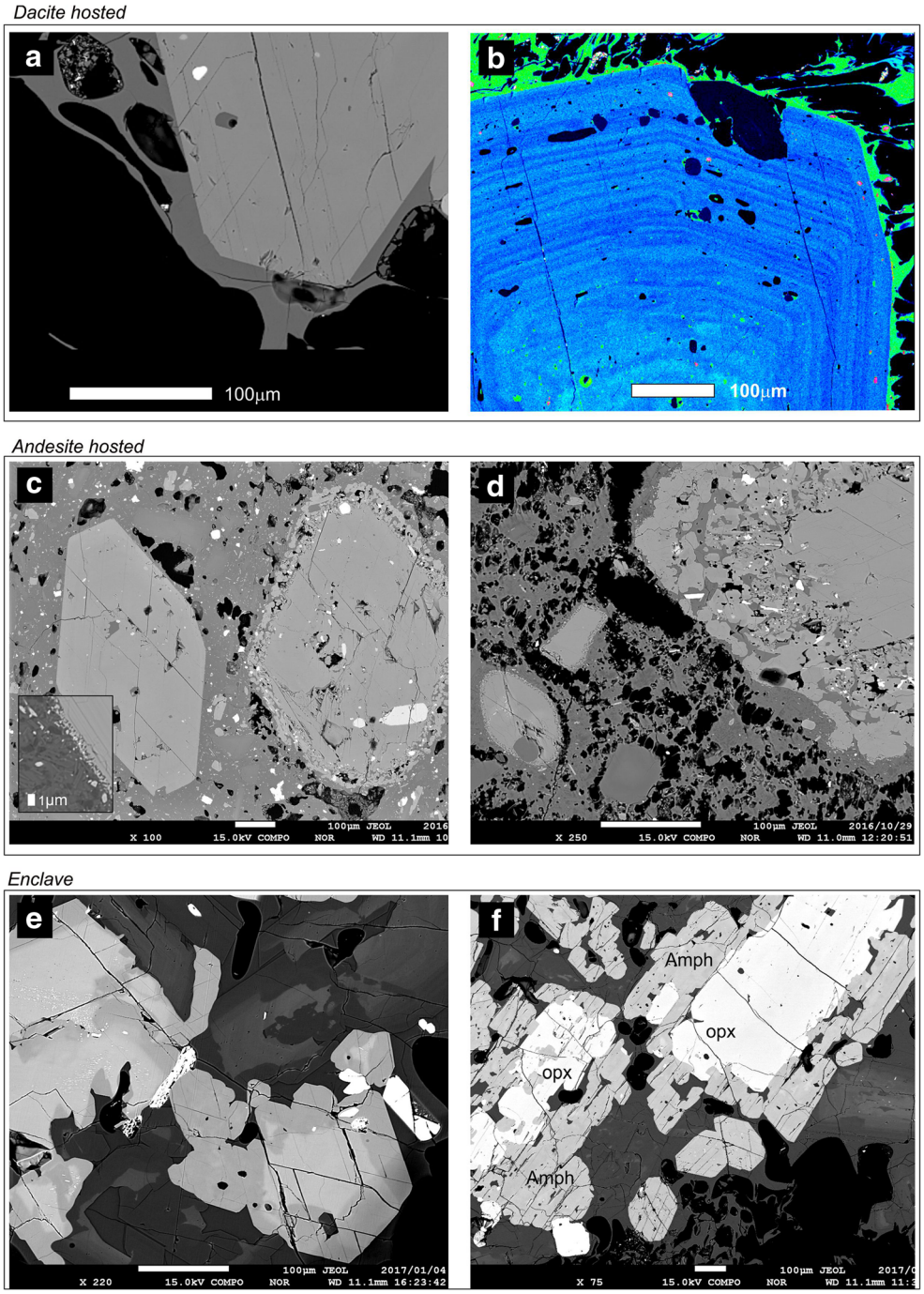

Fig. 9 Textural groups of amphibole. **a** Amphibole in microlite-free dacitic domains without breakdown rims. **b** Al-element map showing subtly, multiple zonation in an oscillatory-zoned amphibole. **c**, **d** Amphibole with clear breakdown rims hosted in the high silica andesite. **e** Amphiboles in mafic enclaves with simple zoning patterns but no high-frequency oscillatory zoning. **f** Thick amphibole overgrowth on orthopyroxene in mafic enclaves

Amphibole-rich mafic enclaves occur frequently in all samples, and their amphiboles are here distinguished as a third textural group. Enclaves are usually composed of plagioclase and amphibole (between 20 and 50%) and variable amounts of Fe–Ti oxides. Zonation is common in enclave amphiboles, but patterns are usually much simpler often showing a distinct compositional variation between core and rim (Fig. 9e). The high-frequency oscillatory zoning patterns (e.g. Fig. 9b) do not occur in these amphiboles. Some of these enclaves also contain subordinate amounts of orthopyroxene and Fe–Ti oxides. If present, orthopyroxene is often affected by thick overgrowth of amphibole (Fig. 9f). If mafic enclaves contain olivine, amphibole is usually absent (see Fig. 8). Amphibole compositions in this third textural group partly overlap with those from groups 1 and 2 but show a considerably larger compositional range. Many of their cores are Tschermakites and are well distinguished from the other types. Substantial variation in the alumina concentration at the tetrahedral site (a—Tschermak exchange) is shown in Fig. 10.

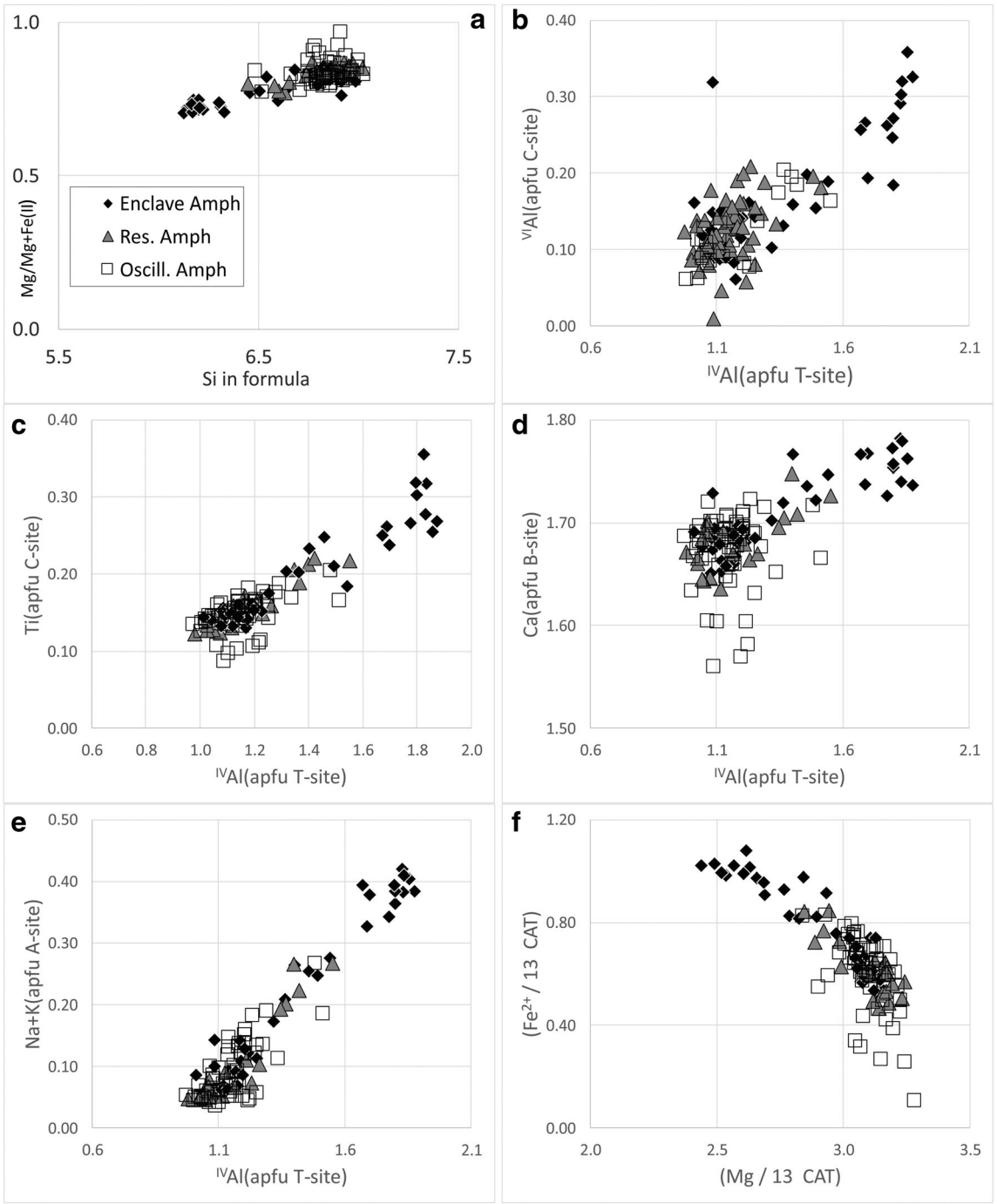

Fig. 10 Amphibole classification and chemistry after Leake (1997). Apfu (atoms per formula unit) showing important coupled substitutions for distinct sites in the amphibole structure. **b** Al-Tschermak exchange. **c** Ti-Tschermak exchange. **d** Plagioclase exchange. **e** Edenite exchange. **f** B site Mg^{2+}/Fe^{2+} exchange

Fe–Ti oxides Fe–Ti oxide minerals are ubiquitous in all samples. They occur as poikillitic inclusions inside Mg–Fe silicate phenocrysts and as individual phenocrysts or small crystal clots. In addition, they form as a breakdown product in some amphiboles and more frequently as symplectites in olivine-bearing mafic enclaves. A limited number of aggregates contain intergrowth of ilmenite and titanomagnetite. Compositions of several touching pairs were determined, and some representative analyses are given in Table 3 and in the electronic supplement.

OPx, olivine and quartz Orthopyroxene is present in small amounts in all samples. Crystals are generally euhedral, unzoned and unresorbed. Compositional variation is very low with Mg# varying only between 63 and 65 for several samples (Online Resource Table ESM 2). Orthopyroxenes in

Table 3 Representative mineral compositions

	Oscillatory	Resorbed	Enclave		Oscillatory	Sieve	Ol Enclave	Olivine		Orthopyroxene			Fe–Ti oxide pair	
	Amph	Amph	Amph		Plag	Plag	Plag		Ol		Opx		Magnetite	Ilmenite
	PF1b_1	PF16_1_77	PF20_10		PF12A_2_31	PF2B_3	PF16_1_56		PF16_1_43		L1A_1_36		L1A_1_35	L1A_1_32
SiO_2	48.291	48.654	41.430		54.978	46.080	45.715		38.770		53.774	SiO_2	0.121	0.080
TiO_2	0.911	1.391	2.409		–	–	–		–		0.091	TiO_2	6.778	38.381
Al_2O_3	7.139	6.932	12.633		29.124	34.653	35.752		0.008		0.468	Al_2O_3	1.935	0.193
FeO	12.562	12.863	15.465		0.343	0.211	0.501		21.839		21.809	FeO	84.768	55.182
MnO	0.508	0.425	0.441		–	–	–		0.657		1.280	MnO	0.534	0.644
MgO	15.232	14.903	11.067		0.008	0.006	0.015		38.830		22.298	MgO	1.040	1.639
CaO	10.480	11.143	10.965		11.038	17.924	18.257		0.007		0.636	CaO	0.000	0.000
Na_2O	1.153	1.173	1.878		4.842	1.398	0.968		–		0.010	Cr_2O_3	0.043	0.031
K_2O	0.227	0.288	0.579		0.221	0.038	0.012		–		0.000	ZnO	0.088	0.000
Total	96.503	97.77	96.867		100.554	100.310	101.220		100.111		100.37	Total	95.307	96.150
Si	6.8962	6.935	6.125	Si	2.465	2.116	2.083	Si	1.005		1.995	Fe_2O_3	54.362	26.821
Al^{IV}	1.1038	1.065	1.875	Al	1.539	1.876	1.920	Ti	–		0.003	FeO	35.853	31.048
Ti	0.0000	0.000	0.000	Fe[II]	0.013	0.008	0.019	Al	0.000		0.020	Total	100.754	98.837
Sum T	8	8	8	Mg	0.001	0.000	0.001	Fe[II]	0.473		0.676			
Al^{VI}	0.0977	0.100	0.326	Ca	0.530	0.882	0.891	Mn	0.014		0.040		Ulvöspinel	Ilmenite
Ti	0.0979	0.149	0.268	Na	0.421	0.124	0.086	Mg	1.501		1.233	∑mol prop:	2.239	1.534
Fe^{3+}	1.2428	0.887	0.892	K	0.013	0.002	0.001	Ca	0.000		0.025	No. of oxygen:	4	3
Mg^{2+}	3.2427	3.167	2.439					Na	–		0.001			
Fe^{2+}	0.2575	0.646	1.019					K	–		0.000	Si	0.005	0.002
Mn	0.0614	0.051	0.055									Ti	0.190	0.737
sum C	5	5	5									Al	0.085	0.006
Mg^{2+}	0.0000	0.000	0.000									Fe+3	1.525	0.515
Fe^{2+}	0.0000	0.000	0.000									Fe+2	1.117	0.663
Mn	0.0000	0.000	0.000									Mn	0.017	0.014
Ca	1.6035	1.702	1.737									Mg	0.058	0.062
Na	0.3192	0.298	0.263									Ca	0.000	0.000
sum B	2	2	2									Cr	0.001	0.001
Na	0.0000	0.026	0.275									Zn	0.002	0.000
K	0.0414	0.052	0.109											
Total	14.9641	15.078	15.384	Total	4.982	5.009	5.000	Total	2.995		3.993	Total	3.000	2.000
										Wo	1.3			
Mg/Mg + Fe(II)	0.9264	0.831	0.705	X_{An}	55.02	87.44	91.18	Fo	76.0	En	62.4			
A site total	0.04	0.08	0.38	X_{Or}	1.31	0.22	0.07	Fa	24.0	Fs	36.3			

amphibole-bearing mafic enclaves often shows overgrowth by amphibole where orthopyroxene cores are preserved at the centre of some amphiboles (Fig. 9f). Orthopyroxene in olivine-bearing enclaves occurs as overgrowth replacing olivine in OPx–Fe–Ti–oxide symplectites (Fig. 8). Here, compositional variation is considerably higher with Mg# varying between 61 and 79. Often, composition changes gradually from the centre to the rim of the mafic enclave (Fig. 8). Temperatures based on the liquid orthopyroxene thermometer of Putirka (2008) have been calculated for several orthopyroxene phenocrysts and are given in Table 3. Olivine occurs at the cores of some mafic enclaves with Mg# between 73 and 77 (Fig. 8, Online Resource Table ESM 2). Quartz occurs in trace amounts as rounded crystals in the dacitic domains (see Fig. 6 overview image).

Discussion

Erupted magma and its storage conditions

Melekestsev et al. (1995) noticed a regular increase in more basic compositions towards younger eruptions at Kizimen. The previous magmatic eruption of the volcano erupted lavas of basaltic andesite composition with 54.5% SiO_2. This trend clearly ended after a long dormancy with the 2010–2013 eruption, which produced the most evolved compositions in the record of Kizimen volcano (Fig. 5). Similar to the earlier eruptive cycles, almost all the erupted products show intricate banding textures between a light and dark component. However, despite the distinctive appearance of both varieties (Fig. 4), the whole rock compositional variation is relatively small ranging from a silica-rich andesite with ~ 62% SiO_2 to a dacite with approximately 65% SiO_2. On a microscopic scale the light toned, overall more evolved glass is translucent, almost free of microphenocrysts and shows a limited compositional range of about 77.5% SiO_2. This is almost identical to values given for the 7550 ^{14}C BP Plinian tephra of Kizimen (Kyle et al. 2011) as well as to the distal ash fallout deposits of the 2010–2013 eruption (Ponomareva et al. 2012). The dark glass is much more microphenocryst and microlith rich and shows a larger compositional range. Previous studies on Kizimen volcano by Browne et al. (2010), as well as the distal tephra record (Kyle et al. 2011; Ponomareva et al. 2012), suggest that a large, stable dacitic magma chamber forms under this volcano during long times of dormancy (Ponomareva et al. 2012). Dacites from this magmatic system will remain in an uneruptible state for most of the time unless mafic recharge is able to activate the system. Such an event is also recorded in the petrography and mineral chemistry of the recent eruption.

Glass and mineral chemistry with respect to their occurrence either in the dacitic bands or in the andesitic bands also shows some distinct characteristics. First, a stable population of oscillatory-zoned plagioclase with an overall limited compositional range and flat, equilibrated trace element profiles is characteristic for the dacitic bands and formed under relatively steady conditions. Regular high-frequency evenly spaced zonation (Fig. 6a–c) probably reflects dynamic fluctuations in the magmatic system (Landi et al. 2004; Ruprecht and Worner 2007; Auer et al. 2013). In contrast, a large number of plagioclases in the andesitic host show sieve-textured interiors and an outer rim of ca 50 μm with substantial higher trace element concentrations which often correlate with anorthite content. However, if preserved (Fig. 6h), cores of resorbed andesite-hosted plagioclases are almost identical to those seen in the dacites with Fe concentrations around 2000 ppm suggesting that these plagioclases were sourced from dacite domain but subsequently affected by magma hybridization related to a mafic recharge. Development of the sieve texture is generally interpreted as a thermal effect (Nakamura and Shimakita 1998), but some plagioclase crystals (Fig. 6d, g) show a sharp increase in An# within their outer rim formed during chemical disequilibrium in contact with mafic melt. Secondly, variation in amphibole textures and composition are shown in Figs. 9 and 10. Again, clearly distinct populations can be identified. Dacite-hosted amphiboles show a narrow compositional range and only subtle oscillatory zonation. In contrast, andesite-hosted amphiboles always show breakdown rims of variable size. However, as for the plagioclases, their cores are practically indistinguishable from those in the dacites.

We used the amphibole thermobarometers of Ridolfi et al. (2010), Ridolfi and Renzulli (2012) and Mutch et al. (2016) to interpret magma storage conditions prior to eruption. Generally, due to the large errors related to the pressure calculation, the applicability of these barometric formulations is under constant critique (Shane and Smith 2013; Erdmann et al. 2014). However, their application has also been supported, for example, under the constrain that it is applied to larger datasets (Putirka 2016). Pressure calculation for the Kizimen amphiboles allows at least an reaffirmation of textural observations and earlier experimental work of Browne (2010) who proposed shallow crustal storage at Kizimen at 125–150 MPa (823 ± 23 °C). Although discrepancies between the individual calibrations are relatively large, all methods yield very similar results when comparing P-T conditions between andesite and dacite-hosted amphiboles yielding a narrow almost identical pressure range for both cases (Table 4). In contrast, amphiboles in mafic enclaves show a much larger compositional variation and crystallized either within a much higher pressure range or during disequilibrium conditions (Shane and Smith 2013; Erdmann et al. 2014; Putirka 2016).

Breakdown rims in amphibole have been used to estimate storage conditions and timescales of magmatic processes on some active volcanoes (Rutherford and Devine 2003; Angelis et al. 2013; Auer et al. 2015, 2016). They occur in many Kizimen samples and can show large variations even for two

Table 4 Estimated intensive variables for the magma produced during the Kizimen 2010–2013 eruption

Method	Type	Host	Number	P_{min} (MPa)	P_{max} (MPa)	P_{av} (MPa)	T (°C)	H_2O_{melt}	ΔNNO
Ridolfi (2010)	Amph-Oscill.	Dacite	60	92	220	123	805	5.7	1.6
	Amph-Resorb.	Andesite	21	86	227	128	809	5.6	1.6
	Amph-Enclave	Cummulate	36	101	464	217	855	6.3	1.1
Ridolfi and Renzulli (2012)	Amph-Oscill.	Dacite	60	114	244	147	805	5.0	0.8
	Amph-Resorb.	Andesite	21	107	239	150	806	4.9	0.4
	Amph-Enclave	Cummulate	36	123	412	217	846	5.5	0.4
Mutch (2016)	Amph-Oscill.	Dacite	60	207	399	261	–	–	–
	Amph-Resorb.	Andesite	21	194	405	266	–	–	–
	Amph-Enclave	Cummulate	36	226	620	371	–	–	–
Putirka (2008)	Opx	Andesite	20	210 [Eq29b]	353 [Eq29b]	290 [Eq29b]	875 Eq28a]	–	–
Ghiorso (2008)	Fe–Ti	Dacite	12	–	–	–	806	–	1.2
	Fe–Ti	Andesite	12	–	–	–	904	–	1.0

adjacent specimens in one sample (Fig. 9c, d). An investigation by De Angelis et al. (2015) tried to establish whether there are textural or compositional differences between amphibole rims formed by decompression versus those formed by heating due to mafic magma recharge. Both cases have found to be almost identical and therefore difficult to relate to a specific process. Because amphibole reaction rims are absent in the dacites but ubiquitous in the andesitic glass, it is likely that these breakdown rims formed during magma hybridization and heating related to mafic recharge.

Temperature and fO_2 for touching pairs of titanomagnetite and ilmenite have been calculated (Table 4) using the thermometers of Ghiorso and Evans (2008) and yield temperatures of about 806 °C for the dacites and 904 °C for the andesites. Orthopyroxene compositions are very uniform, and the mineral occurs in the dacite as well as in the andesite in small amounts. However, mineral-liquid equilibrium for orthopyroxene can only be shown for the andesite. This serves as an additional independent test for the P-T calculations (Putirka 2008) yielding values of 290 MPa and 875 °C for the andesite (Table 4).

In summary, the following points are emphasized. First, although dacitic and andesitic bands are very distinct in appearance—especially at outcrop level (Fig. 4), their actual compositional difference is small and is both among the most evolved compositions in the record of the volcano. Second, plagioclase and amphibole disequilibrium features and reaction textures are ubiquitous in the andesitic bands, but composition of their cores is often identical to those in the dacitic bands. Direct evidence for a mafic recharge event remains elusive and is limited to the almost completely disintegrated cores of olivine (Fig. 8) and the rare high An# anorthite rims on some plagioclases. Instead, we can support a model whereby two distinct mixing events preceded the recent eruption. Initially, there was a mafic recharge event, which most likely stalled at the base of the long-lived dacitic chamber (Fig. 11). This event leads to magma hybridization of an isolated portion in the lower part of the dacitic magma chamber. Whether the hybridization domain remained spatially separated as individual magma pockets from the main dacitic magma chamber (Nakagawa et al. 1999; Dahren et al. 2012; Chadwick et al. 2013), or in a density stratified magma chamber (Blake and Ivey 1986; Nakagawa et al. 2011; Auer et al. 2015), or both, is beyond the resolution of the seismic record or the amphibole thermobarometer. Overall, the effect of the recharge event was rather limited. The majority of the phenocryst cores in the hybrid magma seem to have been initially sourced from the dacitic magma. In addition, the composition of the original dacite magma was set back only slightly to a silica-rich andesite, and a large portion of the dacitic chamber was not affected by this event. It is conceivable that hybridization took a prolonged time, almost completely obliterating direct petrographic evidence of a recharge magma as seen in many of the earlier eruptions (Churikova et al. 2007, 2013a). However, a second mixing event occurred between the silica-rich andesitic hybrid and the dacitic magma just prior to the eruption. Coarse intermingling of these two magmas occurred with negligible thermal and chemical interaction.

A functional model of Kizimen volcano and the mechanism of the 2010–2013 eruption

Magma feeding system

Hypocenters of the precursory earthquakes of the 2010–2013 eruption occupy two distinctive zones: the first one has the shape of a vertical cylinder with a diameter of approximately 3 km located immediately below the volcano, and the second one (located NW from the cylindrical zone) is at the same depth and has the form of a subvertical NE-trending dike (Fig. 3b of Firstov and Shakirova 2014). Both zones extend from the ground surface down to depths of approximately

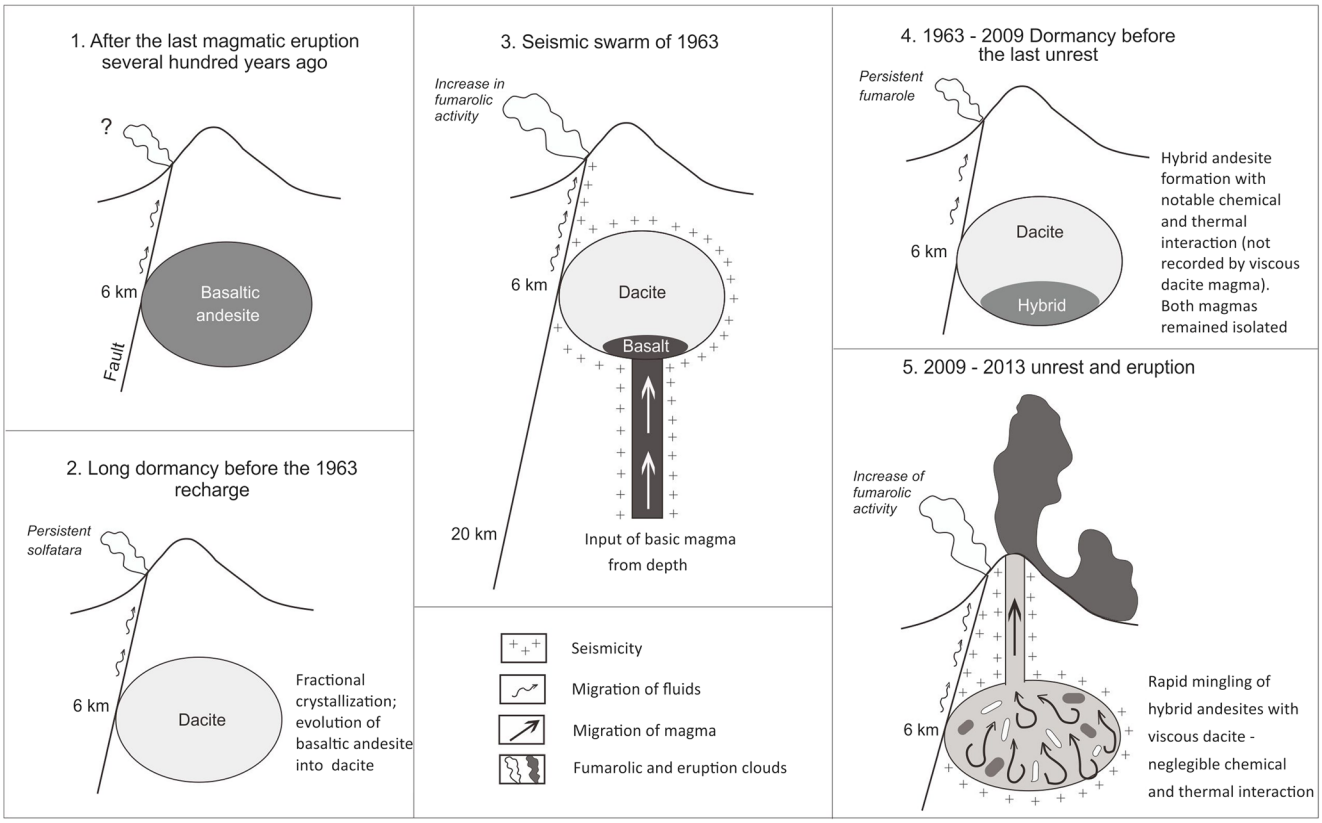

Fig. 11 Functional model of Kizimen volcano

11 km; however, the majority of the earthquakes occurred at depths less than 5 km. The lower part of the cylindrical zone, which has fewer earthquakes on depths between 5 and 11 km, probably locates the silicic magma chamber of the volcano which is in a good agreement with the pressure range calculated from the amphibole and orthopyroxene composition. The upper part of the cylindrical zone, which has a high concentration of earthquakes at depths of less than 5 km, probably marks the path (conduit) along which silicic magma ascended upward to the ground surface. The nearby dike-like zone coincides with an active tectonic fault that crosses the NW flank of the volcano. Seismicity in this zone could be caused by migration of magma or, more likely, by hydrothermal fluids circulating in the fault.

The schematic geometry of the magma feeding system of Kizimen and its possible dynamics is shown in Fig. 11. According to petrological data from earlier eruptions, the shallow silicic magma system of Kizimen is fed periodically by high-magnesium basic magma ascending from a deeper source (Churikova et al. 2007, 2013a). Such magma ascends from a depth of more than 20 km, as is known for the nearby Tolbachik volcano (Belousov et al. 2015a). The absence of deep (> 11 km) earthquakes in the seismic data that preceded and accompanied the 2010–2013 eruption of Kizimen indicates that this event was not directly triggered and/or accompanied by the input of basic magma from a greater depth. This is also supported by our petrological studies where unlike in many of the earlier eruption products (Churikova et al. 2007), we have not found large enclaves of basaltic or basaltic andesite composition. However, such input may have occurred in 1963 when an intensive seismic swarm was registered under Kizimen (with no eruption) with earthquakes at depths ranging from 0 to more than 35 km (Senyukov et al. 2011). If this assumption is correct, and no further recharge occurred during the following time, it took 47 years for the newly injected mafic magma to form a high silica andesitic hybrid which reached an eruptible state in 2009. The most likely cause of this prolonged duration is the substantial vertical extent of the dacitic magma chamber and its role as a density filter (Blake and Ivey 1986; Kent et al. 2010; Auer et al. 2015). Small batches of ascending basaltic magma will have too high density to traverse the existing magmatic system, but too little thermal energy to quickly bring the dacitic reservoir into an eruptible state. While magma mixing will eventually lower the density of the hybrid magma sufficiently to further rise and traverse the highly evolved magma body, coarse mingling with the highly viscous dacite will also occur (Fig. 11).

InSAR data reveal ground deformations preceding the eruption. These were interpreted as being induced by intrusion of magma in a form of long and thin dike (Ji et al. 2013). We believe that this interpretation does not fit the existing geological and seismological data. The lower, deeper half of the

suggested dike is not marked by hypocentres of the earthquake swarm (Fig. 7 of Ji et al. 2013), and it is difficult to agree with Ji et al. (2013) that at depths of 12–18 km, such intrusion could occur aseismically. In this regard, in a similar geologic and tectonic situation at the nearby Tolbachik volcano, intrusion of dikes generates multiple earthquakes at depths of up to 30 km. We think that the observed ground deformations could thus be caused, in part, by the increase of fluid pore pressure along the plane of the tectonic fault associated with the nearby magma intrusion. Probably, the registered ground deformation would be better modelled as some combination of a fault plane with increased pore pressure and a vertical cylinder beneath the volcano at depths < 11 km (i.e. in the pressurized silicic magma chamber).

Eruption scenarios and mechanisms

In the Late Holocene history of Kizimen, there were few highly explosive events involving the eruption of highly vesiculated magma (Melekestsev et al. 1995); the edifice is composed mostly of domes and thick lava flows. The most common eruption scenario for this volcano thus represents slow extrusion of highly viscous, partly degassed silica-rich magma accompanied by only moderate explosive activity (intensive phreatomagmatic explosive activity, however, is possible during initial periods of an eruption). Hence, the scenario of the 2010–2013 eruption can be considered as typical for Kizimen. On volcanoes with similar magma compositions, an eruption commonly starts with a highly explosive Plinian stage (producing essentially pumice) that is later followed by extrusion of degassed lava (Gorshkov 1959; Lipman and Mullineaux 1981; Belousov 1995). The question thus arises: why are such Plinian explosive stages rather weak, or even absent, at Kizimen—as was observed in the course of the recent eruption? To answer this question, we suggest that silicic magma at Kizimen partly degasses long before eruption, during residence in the shallow magmatic system (Fig. 11). Magmatic fluids probably leak through the active tectonic fault zone that crosses the edifice, and probably the magma chamber as well. At the ground surface, this leakage is apparent as the persistent fumarole on the NW flank of the volcano. The fumarole is located 600 m upslope from the escarpment of the major fault; thus, in its upper part, the leakage path probably follows one of the secondary arcuate faults that form when a major fault crosses a volcanic cone (Merle et al. 2001; Belousov et al. 2005). The fact that activity of this fumarole was not disrupted by the recent eruption clearly indicates that the paths of migration of volatiles and magma do not coincide at Kizimen (Fig. 11). In part, the leaking fluids probably dissolve in underground waters circulating within the fault zone and which form two groups of thermal springs located along the major fault in the valley of the Levaya Schapina river.

Degassing causes notable depressurization and increase in viscosity of the silicic magma in the chamber (Girona et al. 2014, 2015). This process decreases the dynamic of the dacitic magma chamber, acting as a density filter. At the same time, the process prevents the dacitic magma itself from reaching an eruptible state. Once unrest begins, the high viscosity of the magma leads to an unusually long period of pre-eruption seismicity (which lasted ~ 1.5 years before the onset of the eruption in 2010), incomplete intermixing of the magma components (to result in eruption of banded andesites and dacites) and high viscosity of the extruded lava ($> 10^{10}$ Pa s). Geological data show that highly viscous magma was common for many of the previous prehistoric eruptions of the volcano (Piip 1946; Melekestsev et al. 1995; Churikova et al. 2007).

High viscosity of the erupting magma and location of the volcano on the active tectonic fault makes future large-scale gravitational failure of the volcanic edifice very likely, as was mentioned by Melekestsev et al. (1995). The character of explosive activity (lateral blast or vertical Plinian eruption) accompanying such gravitational unloading will depend on the depth of magma inside the volcanic edifice in the moment of failure (Belousov et al. 2007).

Conclusion

Kizimen has three remarkable geological features: (1) the volcano sits directly on the active regional tectonic fault; (2) it repeatedly erupts viscous andesitic-dacitic magmas with relatively low explosivity; and (3) its magmas are highly heterogeneous and poorly intermingled. Our investigations allow us to suggest that these features are linked to each other. The fault zone probably serves as a path for continuous leakage of volatiles from the shallow silicic magma chamber. This process feeds strong and persistent fumarole on the NW flank of the volcano. Such long-term passive degassing depressurizes the magma chamber, increases the viscosity of magma in the shallow chamber and lowers the explosivity of its eruptions. The increased viscosity in turn prevents thorough intermixing between the silicic magma and acts as an efficient density filter for mafic magmas ascending from depth. High viscosity of magma in the chamber can be responsible for the long time periods between the input of the basic magma into the system (that probably occurred in 1963) and the following eruptions (which, in our case, occurred in 2010). Eruption of such viscous and degassed magma produces thick lava flows and domes. Lava flow formed during the recent eruption of Kizimen is remarkable for dacitic volcanoes for its high viscosity ($> 10^{10}$ Pa s), thickness (> 200 m) and volume (0.3 km^3). The collected data about the flow dynamics are among the few others that exist for such voluminous silicic flows (Silva et al. 1994; Harris et al. 2004).

An important observation for the future forecasts of eruptions at Kizimen is that a swarm of deep (> 30 km) earthquakes can indicate an input of basic magma into the shallow silicic chamber without immediate eruption. The delay between such an input and the following eruption for this volcano can last for many decades, in this case five decades. In contrast, a swarm of shallow earthquakes (< 10 km) can indicate that magma in the chamber has reached an eruptible state and has begun to ascend towards the surface. Due to the high viscosity of the ascending magma, shallow earthquake swarms preceding eruptions of Kizimen can last for more than a year as the magma slowly breaks a pathway to the surface. Similar processes possibly occur at other persistently degassing volcanoes with highly evolved magmas, as at Tatun in Taiwan and Gede in Java, Indonesia (Belousov et al. 2010, 2015b), Sinabung (Nakada et al. 2017) and Mayon (Global Volcanism Program 2016).

Acknowledgements Basic funding for this research was provided by the Institute of Volcanology and Seismology of the Russian Academy of Sciences (to AB and MB). Our field work at Kizimen volcano in 2012 was funded in part by the NASA "Science of Terra and Aqua" Research Program (NNX14AQ96G) grant to Mike Ramsey. We are also grateful to Mike Ramsey and Steve Anderson for the support and fruitful scientific discussions during the field work. The field work was conducted with permission of the Kronotsky Natural Reserve. We also thank the Kamchatkan Branch of the Russian Geophysical Survey for the time-lapse footage of the eruption obtained with their monitoring camera.

References

Angelis D, H S LJ, Coombs M (2013) Pre-eruptive magmatic conditions at Augustine volcano, Alaska, 2006: evidence from amphibole geochemistry and textures. J Petrol 54(9):1939–1961. https://doi.org/10.1093/petrology/egt037

Auer A, White JDL, Nakagawa M, Rosenberg MD (2013) Petrological record from young Ruapehu eruptions in the 4.5 ka Kiwikiwi Formation, Whangaehu Gorge, New Zealand. N Z J Geol Geophys 56(3):121–133. https://doi.org/10.1080/00288306.2013.796998

Auer A, Martin CE, Palin JM, White JDL, Nakagawa M, Stirling C (2015) The evolution of hydrous magmas in the Tongariro Volcanic Centre: the 10 ka Pahoka-Mangamate eruptions. N Z J Geol Geophys 58(4):364–384. https://doi.org/10.1080/00288306.2015.1089913

Auer A, White JDL, Tobin MJ (2016) Variable H2O content in magmas from the Tongariro Volcanic Centre and its relation to crustal storage and magma ascent. J Volcanol Geotherm Res 325:203–210. https://doi.org/10.1016/j.jvolgeores.2016.06.021

Bachmann O, Dungan MA (2002) Temperature-induced Al-zoning in hornblendes of the Fish Canyon magma, Colorado. Am Mineral 87(8-9):1062–1076. https://doi.org/10.2138/am-2002-8-903

Belousov AB (1995) The Shiveluch volcanic eruption of 12 November 1964—explosive eruption provoked by failure of the edifice. J Volcanol Geotherm Res 66(1-4):357–365. https://doi.org/10.1016/0377-0273(94)00072-O

Belousov A, Voight B, Belousova M, Petukhin A (2002) Pyroclastic surges and flows from the 8-10 May 1997 explosive eruption of Bezymianny volcano, Kamchatka, Russia. Bull Volcanol 64(7):455–471. https://doi.org/10.1007/s00445-002-0222-5

Belousov A, Walter TR, Troll VR (2005) Large-scale failures on domes and stratocones situated on caldera ring faults: sand-box modeling of natural examples from Kamchatka, Russia. Bull Volcanol 67(5):457–468. https://doi.org/10.1007/s00445-004-0387-1

Belousov A, Voight B, Belousova M (2007) Directed blasts and blast-generated pyroclastic density currents: a comparison of the Bezymianny 1956, Mount St Helens 1980, and Soufrière Hills, Montserrat 1997 eruptions and deposits. Bull Volcanol 69(7):701–740. https://doi.org/10.1007/s00445-006-0109-y

Belousov A, Belousova M, Chen C-H, Zellmer GF (2010) Deposits, character and timing of recent eruptions and gravitational collapses in Tatun Volcanic Group, Northern Taiwan: hazard-related issues. J Volcanol Geotherm Res 191(3-4):205–221. https://doi.org/10.1016/j.jvolgeores.2010.02.001

Belousov A, Belousova M, Edwards B et al (2015a) Overview of the precursors and dynamics of the 2012–13 basaltic fissure eruption of Tolbachik Volcano, Kamchatka, Russia. J Volcanol Geotherm Res 307:22–37

Belousov A, Belousova M, Krimer D et al (2015b) Volcaniclastic stratigraphy of Gede Volcano, West Java, Indonesia: how it erupted and when. J Volcanol Geotherm Res 301:238–252

Blake S, Ivey GN (1986) Magma-mixing and the dynamics of withdrawal from stratified reservoirs. J Volcanol Geotherm Res 27(1-2):153–178. https://doi.org/10.1016/0377-0273(86)90084-3

Blundy J, Cashman K, Humphreys M (2006) Magma heating by decompression-driven crystallization beneath andesite volcanoes. Nature 443(7107):76–80. https://doi.org/10.1038/nature05100

Browne BL, Eichelberger JC, Patino LC, Vogel TA, Uto K, Hoshizumi H (2006) Magma mingling as indicated by texture and Sr/Ba ratios of plagioclase phenocrysts from Unzen volcano, SW Japan. J Volcanol Geotherm Res 154(1-2):103–116. https://doi.org/10.1016/j.jvolgeores.2005.09.022

Browne B, Izbekov P, Eichelberger J, Churikova T (2010) Pre-eruptive storage conditions of the Holocene dacite erupted from Kizimen volcano, Kamchatka. Int Geol Rev 52(1):95–110. https://doi.org/10.1080/00206810903332413

Carmichael ISE (1967) The iron-titanium oxides of salic volcanic rocks and their associated ferromagnesian silicates. Contrib Mineral Petrol 14(1):36–64. https://doi.org/10.1007/BF00370985

Chadwick JP, Troll VR, Waight TE, van der Zwan FM, Schwarzkopf LM (2013) Petrology and geochemistry of igneous inclusions in recent Merapi deposits: a window into the sub-volcanic plumbing system. Contrib Mineral Petrol 165(2):259–282. https://doi.org/10.1007/s00410-012-0808-7

Churikova T, Wörner G, Eichelberger J, Ivanov B (2007) Minor-and trace element zoning in plagioclase from Kizimen volcano, Kamchatka: insights on the magma chamber processes. Volcanism Subduction Kamchatka Reg:303–323. https://doi.org/10.1029/172GM22

Churikova T, Wörner G, Eichelberger J, Ivanov B (2013a) Minor- and trace element zoning in plagioclase from Kizimen volcano, Kamchatka: insights on the magma chamber processes. In: Eichelberger J, Gordeev E, Izbekov P et al (eds) Volcanism and Subduction: The Kamchatka Region. American Geophysical Union, Washington, D.C., pp 303–323

Churikova TG, Ivanov BV, Eichelberger J, Wörner G, Browne B, Izbekov P (2013b) Major and trace element zoning in plagioclase from Kizimen volcano (Kamchatka): insights into magma-chamber processes. J Volcanol Seismol 7(2):112–130. https://doi.org/10.1134/S0742046313020024

Crabtree SM, Lange RA (2011) Complex phenocryst textures and zoning patterns in andesites and dacites: evidence of degassing-induced rapid crystallization? J Petrol 52(1):3–38. https://doi.org/10.1093/petrology/egq067

Dahren B, Troll VR, Andersson UB, Chadwick JP, Gardner MF, Jaxybulatov K, Koulakov I (2012) Magma plumbing beneath Anak Krakatau volcano, Indonesia: evidence for multiple magma storage regions. Contrib Mineral Petrol 163(4):631–651. https://doi.org/10.1007/s00410-011-0690-8

De Angelis SH, Larsen J, Coombs M et al (2015) Amphibole reaction rims as a record of pre-eruptive magmatic heating: an experimental approach. Earth Planet Sci Lett 426:235–245

Dougal AJ, Martin MM (2008) Understanding crystal populations and their significance through the magmatic plumbing system. Geol Soc Lond Spec Publ 304:133–148

Dvigalo VN, Melekestsev IV, Shevchenko AV, Svirid IY (2013) The 2010–2012 eruption of Kizimen volcano: the greatest output (from the data of remote-sensing observations) for eruptions in Kamchatka in the early 21st century part I. The November 11, 2010 to December 11, 2011 phase. J Volcanol Seismol 7(6):345–361. https://doi.org/10.1134/S074204631306002X

Eichelberger JC (1975) Origin of andesite and dacite—evidence of mixing at glass mountain in california and at other circum-pacific volcanos. Geol Soc Am Bull 86(10):1381–1391. https://doi.org/10.1130/0016-7606(1975)86<1381:OOAADE>2.0.CO;2

Erdmann S, Martel C, Pichavant M, Kushnir A (2014) Amphibole as an archivist of magmatic crystallization conditions: problems, potential, and implications for inferring magma storage prior to the paroxysmal 2010 eruption of Mount Merapi, Indonesia. Contrib Mineral Petrol 167(6):1016. https://doi.org/10.1007/s00410-014-1016-4

Firstov PP, Shakirova AA (2014) Seismicity observed during the precursory process and the actual eruption of Kizimen volcano, Kamchatka in 2009–2013. J Volcanol Seismol 8(4):203–217. https://doi.org/10.1134/S0742046314040022

Gauthier F (1973) Field and laboratory studies of the rheology of Mount Etna lava. Philos Trans R Soc Lond Ser Math Phys Sci 274(1238):83–98. https://doi.org/10.1098/rsta.1973.0028

Ghiorso MS, Evans BW (2008) Thermodynamics of rhombohedral oxide solid solutions and a revision of the Fe-Ti two-oxide geothermometer and oxygen-barometer. Am J Sci 308(9):957–1039. https://doi.org/10.2475/09.2008.01

Gill J (1981) Orogenic andesites and plate tectonics. Springer, Berlin. https://doi.org/10.1007/978-3-642-68012-0

Girona T, Costa F, Newhall C, Taisne B (2014) On depressurization of volcanic magma reservoirs by passive degassing. J Geophys Res Solid Earth 119:8667–8687

Girona T, Costa F, Schubert G (2015) Degassing during quiescence as a trigger of magma ascent and volcanic eruptions. Sci Rep 5(1):18212. https://doi.org/10.1038/srep18212

Global Volcanism Program (2016) Report on Mayon (Philippines). In: Venzke E (ed) Bulletin of the Global Volcanism Network, 41:3. Smithsonian Institution, Washington, DC

Gorshkov GS (1959) Gigantic eruption of the volcano Bezymianny. Bull Volcanol 20(1):77–109. https://doi.org/10.1007/BF02596572

Hackett WR, Houghton BF (1989) A facies model for a quaternary andesitic composite volcano: Ruapehu, New Zealand. Bull Volcanol 51(1):51–68. https://doi.org/10.1007/BF01086761

Hammer JE, Rutherford MJ (2002) An experimental study of the kinetics of decompression-induced crystallization in silicic melt. J Geophys Res Solid Earth 107(B1):ECV 8-1–ECV 8-24. https://doi.org/10.1029/2001JB000281

Harris AJ, Rowland SK (2015) Lava flows and rheology. In: The Encyclopedia of Volcanoes, 2nd edn. Elsevier, Amsterdam, pp 321–342. https://doi.org/10.1016/B978-0-12-385938-9.00017-1

Harris AJL, Flynn LP, Matias O, Rose WI, Cornejo J (2004) The evolution of an active silicic lava flow field: an ETM+ perspective. J Volcanol Geotherm Res 135(1-2):147–168. https://doi.org/10.1016/j.jvolgeores.2003.12.011

Hattori K, Sato H (1996) Magma evolution recorded in plagioclase zoning in 1991 Pinatubo eruption products. Am Mineral 81:982–994. https://doi.org/10.2138/am-1996-7-820

Hoblitt RP, Harmon RS (1993) Bimodal density distribution of cryptodome dacite from the 1980 eruption of Mount St. Helens, Washington. Bull Volcanol 55(6):421–437. https://doi.org/10.1007/BF00302002

Houghton BF, Wilson CJN (1989) A vesicularity index for pyroclastic deposits. Bull Volcanol 51(6):451–462. https://doi.org/10.1007/BF01078811

Humphreys MCS, Blundy JD, Sparks RSJ (2006a) Magma evolution and open-system processes at Shiveluch volcano: insights from phenocryst zoning. J Petrol 47(12):2303–2334. https://doi.org/10.1093/petrology/egl045

Humphreys MCS, Kearns SL, Blundy JD (2006b) SIMS investigation of electron-beam damage to hydrous, rhyolitic glasses: implications for melt inclusion analysis. Am Mineral 91(4):667–679. https://doi.org/10.2138/am.2006.1936

Izbekov PE, Eichelberger JC, Patino LC, Vogel TA, Ivanov BV (2002) Calcic cores of plagioclase phenocrysts in andesite from Karymsky volcano: evidence for rapid introduction by basaltic replenishment. Geology 30(9):799–802. https://doi.org/10.1130/0091-7613(2002)030<0799:CCOPPI>2.0.CO;2

Jeffreys H (1925) The flow of water in an inclined channel of rectangular section. Lond Edinb Dublin Philos Mag J Sci 49:793–807

Ji L, Lu Z, Dzurisin D, Senyukov S (2013) Pre-eruption deformation caused by dike intrusion beneath Kizimen volcano, Kamchatka, Russia, observed by InSAR. J Volcanol Geotherm Res 256:87–95. https://doi.org/10.1016/j.jvolgeores.2013.02.011

Jolly AD, Sherburn S, Jousset P, Kilgour G (2010) Eruption source processes derived from seismic and acoustic observations of the 25 September 2007 Ruapehu eruption-North Island, New Zealand. J Volcanol Geotherm Res 191(1-2):33–45. https://doi.org/10.1016/j.jvolgeores.2010.01.009

Kent AJ, Koleszar AM, Darr C et al (2010) Preferential eruption of andesitic magmas through recharge filtering. Nat Geosci 3(9):631–636. https://doi.org/10.1038/ngeo924

Kilgour G, Blundy J, Cashman K, Mader HM (2013) Small volume andesite magmas and melt–mush interactions at Ruapehu, New Zealand: evidence from melt inclusions. Contrib Mineral Petrol 166(2):371–392. https://doi.org/10.1007/s00410-013-0880-7

Kilgour GN, Saunders KE, Blundy JD, Cashman KV, Scott BJ, Miller CA (2014) Timescales of magmatic processes at Ruapehu volcano from diffusion chronometry and their comparison to monitoring data. J Volcanol Geotherm Res 288:62–75. https://doi.org/10.1016/j.jvolgeores.2014.09.010

Kimura J, Yamada Y (1996) Evaluation of major and trace element XRF analyses using a flux to sample ratio of two to one glass beads. J Mineral Petrol Econ Geol 91(2):62–72. https://doi.org/10.2465/ganko.91.62

Kirsanova TP, Yurova LM, Vergasova LP, Taran YA (1983) Fumarolic activity of Shiveluch and Kizimen volcanoes in 1979–1980. Volcanol Seism 3:33–43

Kyle PR, Ponomareva VV, Rourke Schluep R (2011) Geochemical characterization of marker tephra layers from major Holocene eruptions, Kamchatka Peninsula, Russia. Int Geol Rev 53(9):1059–1097. https://doi.org/10.1080/00206810903442162

Landi P, Métrich N, Bertagnini A, Rosi M (2004) Dynamics of magma mixing and degassing recorded in plagioclase at Stromboli (Aeolian archipelago, Italy). Contrib Mineral Petrol 147(2):213–227. https://doi.org/10.1007/s00410-004-0555-5

Lautze NC, Houghton BF (2007) Linking variable explosion style and magma textures during 2002 at Stromboli Volcano, Italy. Bull Volcanol 69(4):445–460. https://doi.org/10.1007/s00445-006-0086-1

Leake BE, Woolley AR, Arps CE et al (1997) Report. Nomenclature of amphiboles: report of the subcommittee on amphiboles of the international mineralogical association commission on new minerals and mineral names. Mineral Mag 61(405):295–321. https://doi.org/10.1180/minmag.1997.061.405.13

Lipman PW, Mullineaux DR (1981) The 1980 eruptions of Mount St. Helens, Washington. US Dept. of the Interior, US Geological Survey, Reston

Malik NA (2015) Eruption of Kizimen volcano in 210-2013: results of investigations of soluble elements from ash, water and gas. Conf Volcanism Relat Process Petropavlovsk-Kamchatsky Russ 84–91 (in Russian)

Malik NA, Ovsyannikov AA (2011) The eruption of Kizimen volcano from October 2010 to March 2011. Bull Kamchatka Assoc "Educational-Sci Center" Earth Sci 7–10 (in Russian)

Martel C, Pichavant M, Bourdier JL et al (1998) Magma storage conditions and control of eruption regime in silicic volcanoes: experimental evidence from Mt. Pelee. Earth Planet Sci Lett 156(1-2):89–99. https://doi.org/10.1016/s0012-821x(98)00003-x

Melekestsev IV, Ponomareva VV, Volynets ON (1995) Kizimen volcano, Kamchatka—a future Mount St. Helens? J Volcanol Geotherm Res 65(3-4):205–226. https://doi.org/10.1016/0377-0273(94)00082-R

Melnikov DV, Dvigalo DV, Melekestsev IV (2011) The 2010–2011 eruption of Kizimen volcano, Kamchatka: dynamics of eruptive activity and geologic-geomorphological impact (based on remote sensing data). Bull Kamchatka Assoc "Educational-Sci Center" Earth Sci 85–99 (in Russian)

Merle O, Vidal N, van Wyk de Vries B (2001) Experiments on vertical basement fault reactivation below volcanoes. J Geophys Res Solid Earth 106(B2):2153–2162. https://doi.org/10.1029/2000JB900352

Métrich N, Bertagnini A, Landi P, Rosi M (2001) Crystallization driven by decompression and water loss at Stromboli Volcano (Aeolian Islands, Italy). J Petrol 42(8):1471–1490. https://doi.org/10.1093/petrology/42.8.1471

Miyashiro A (1974) Volcanic rock series in island arcs and active continental margins. Am J Sci 274(4):321–355. https://doi.org/10.2475/ajs.274.4.321

Mueller S, Scheu B, Kueppers U, Spieler O, Richard D, Dingwell D (2011) The porosity of pyroclasts as an indicator of volcanic explosivity. J Volcanol Geotherm Res 203(3-4):168–174. https://doi.org/10.1016/j.jvolgeores.2011.04.006

Mutch EJF, Blundy JD, Tattitch BC, Cooper FJ, Brooker RA (2016) An experimental study of amphibole stability in low-pressure granitic magmas and a revised Al-in-hornblende geobarometer. Contrib Mineral Petrol 171(10):85. https://doi.org/10.1007/s00410-016-1298-9

Nakada S, Shimizu H, Ohta K (1999) Overview of the 1990–1995 eruption at Unzen volcano. J Volcanol Geotherm Res 89:1–22

Nakada S, Zaennudin A, Yoshimoto M, et al (2017) Growth process of the lava dome/flow complex at Sinabung volcano during 2013–2016. J Volcanol Geotherm Res. https://doi.org/10.1016/j.jvolgeores.2017.06.012

Nakagawa M, Wada K, Thordarson T et al (1999) Petrologic investigations of the 1995 and 1996 eruptions of Ruapehu volcano, New Zealand: formation of discrete and small magma pockets and their intermittent discharge. Bull Volcanol 61:15–31

Nakagawa M, Hiraga N, Furukawa R (2011) Formation of a zoned magma chamber and its temporal evolution during the historic eruptive activity of Tarumai volcano, Japan: petrological implications for a long-term forecast of eruptive activity of an active volcano. J Volcanol Geotherm Res 205(1-2):1–16. https://doi.org/10.1016/j.jvolgeores.2011.05.003

Nakamura M, Shimakita S (1998) Dissolution origin and syn-entrapment compositional change of melt inclusion in plagioclase. Earth Planet Sci Lett 161(1-4):119–133. https://doi.org/10.1016/s0012-821x(98)00144-7

Nichols RL (1939) Viscosity of lava. J Geol 47(3):290–302. https://doi.org/10.1086/624778

Piip BI (1946) Kizimen volcano. Bull Volcanol Stn:22–32 (in Russian)

Ponomareva VV, Portnyagin MV, Melnikov DV (2012) Composition of tephra of modern (2009-2011) eruptions of Kamchatka and Kurile islands. Bull Kamchatka Assoc "Educational-Sci Center" Earth Sci 23–37 (in Russian)

Putirka KD (2008) Thermometers and barometers for volcanic systems. In: Putirka KD, Tepley FJ (eds) Minerals, Inclusions and Volcanic Processes. Mineralogical Soc Amer, Chantilly, pp 61–120

Putirka K (2016) Special collection: rates and depths of magma ascent on earth: amphibole thermometers and barometers for igneous systems and some implications for eruption mechanisms of felsic magmas at arc volcanoes. Am Mineral 101(4):841–858. https://doi.org/10.2138/am-2016-5506

Pyle DM (2015) Sizes of volcanic eruptions. In: The Encyclopedia of Volcanoes, 2nd edn. Elsevier, Amsterdam, pp 257–264. https://doi.org/10.1016/B978-0-12-385938-9.00013-4

Ridolfi F, Renzulli A (2012) Calcic amphiboles in calc-alkaline and alkaline magmas: thermobarometric and chemometric empirical equations valid up to 1,130° C and 2.2 GPa. Contrib Mineral Petrol 163(5):877–895. https://doi.org/10.1007/s00410-011-0704-6

Ridolfi F, Renzulli A, Puerini M (2010) Stability and chemical equilibrium of amphibole in calc-alkaline magmas: an overview, new thermobarometric formulations and application to subduction-related volcanoes. Contrib Mineral Petrol 160(1):45–66. https://doi.org/10.1007/s00410-009-0465-7

Ruprecht P, Bachmann O (2010) Pre-eruptive reheating during magma mixing at Quizapu volcano and the implications for the explosiveness of silicic arc volcanoes. Geology 38(10):919–922. https://doi.org/10.1130/G31110.1

Ruprecht P, Worner G (2007) Variable regimes in magma systems documented in palgioclase zoning patterns: El Misti stratovolcano and Andahua monogenetic cones. J Volcanol Geotherm Res 165(3-4):142–162. https://doi.org/10.1016/j.jvolgeores.2007.06.002

Ruprecht P, Bergantz GW, Cooper KM, Hildreth W (2012) The crustal magma storage system of Volcán Quizapu, Chile, and the effects of magma mixing on magma diversity. J Petrol 53(4):801–840. https://doi.org/10.1093/petrology/egs002

Rutherford MJ, Devine JD (2003) Magmatic conditions and magma ascent as indicated by hornblende phase equilibria and reactions in the 1995–2002 Soufrière Hills magma. J Petrol 44(8):1433–1453. https://doi.org/10.1093/petrology/44.8.1433

Scaillet B, Evans BW (1999) The 15 June 1991 eruption of Mount Pinatubo. I. Phase equilibria and pre-eruption P-T-fO(2)-fH(2)O conditions of the dacite magma. J Petrol 40(3):381–411. https://doi.org/10.1093/petrology/40.3.381

Senyukov SL, Nuzhdina IN, Droznina SY (2011) The seismicity of Kizimen volcano. Probl Complex Geophys Monit Far East Russ 144–148 (in Russian)

Shane P, Smith VC (2013) Using amphibole crystals to reconstruct magma storage temperatures and pressures for the post-caldera collapse volcanism at Okataina volcano. Lithos 156–159:159–170. https://doi.org/10.1016/j.lithos.2012.11.008

Shantser AY, Kutyev FS, Petrov VS, Zubin MI (1991) Kizimen volcano. In: Fedotov SA, Masurenkov YP (eds) Active volcanoes of Kamchatka. Nauka, Moscow 2:28

Shcherbakov VD, Plechov PY, Izbekov PE, Shipman JS (2011) Plagioclase zoning as an indicator of magma processes at Bezymianny volcano, Kamchatka. Contrib Mineral Petrol 162(1):83–99. https://doi.org/10.1007/s00410-010-0584-1

Shea T, Gurioli L, Larsen JF et al (2010) Linking experimental and natural vesicle textures in Vesuvius 79AD white pumice. J Volcanol

Geotherm Res 192(1-2):69–84. https://doi.org/10.1016/j.jvolgeores.2010.02.013

Silva S de, Self S, Francis PW et al (1994) Effusive silicic volcanism in the Central Andes: The Chao dacite and other young lavas of the Altiplano-Puna Volcanic Complex. J Geophys Res Solid Earth 99: 17805–17825

Sparks RSJ, Cashman KV (2017) Dynamic magma systems: implications for forecasting volcanic activity. Elements 13(1):35–40. https://doi.org/10.2113/gselements.13.1.35

Tembrel II, Ovsyannikov AA (2009) Activity of Kizimen volcano at summer 2009. Bull Kamchatka Assoc "Educational-Sci Center". Earth Sci 14:7–9 (in Russian)

Trusov SV, Pletchov PY (2011) Physico-chemical parameters of magma chamber under Kizimen volcano. 7th Bienn Workshop Jpn-Kamchatka-Alsk Subduction Process 182–183

Walker GPL (1971) Grain-size characteristics of pyroclastic deposits. J Geol 79(6):696–714. https://doi.org/10.1086/627699

Yamamoto M, Kawakatsu H, Yomogida K, Koyama J (2002) Long-period (12 sec) volcanic tremor observed at Usu 2000 eruption: seismological detection of a deep magma plumbing system. Geophys Res Lett 29(9):4–43-4. https://doi.org/10.1029/2001gl013996

Young SR, Sparks RSJ, Aspinall WP, Lynch LL, Miller AD, Robertson REA, Shepherd JB (1998) Overview of the eruption of Soufriere Hills volcano, Montserrat, 18 July 1995 to December 1997. Geophys Res Lett 25(18):3389–3392. https://doi.org/10.1029/98GL01405